

## Pareto-based modulated model predictive control strategy for power converter applications

Santis, Patricio; Sáez, Doris; Cárdenas, Roberto; Núñez, Alfredo

**DOI**

[10.1016/j.epsr.2019.02.016](https://doi.org/10.1016/j.epsr.2019.02.016)

**Publication date**

2019

**Document Version**

Accepted author manuscript

**Published in**

Electric Power Systems Research

**Citation (APA)**

Santis, P., Sáez, D., Cárdenas, R., & Núñez, A. (2019). Pareto-based modulated model predictive control strategy for power converter applications. *Electric Power Systems Research*, 171, 158-174. <https://doi.org/10.1016/j.epsr.2019.02.016>

**Important note**

To cite this publication, please use the final published version (if applicable). Please check the document version above.

**Copyright**

Other than for strictly personal use, it is not permitted to download, forward or distribute the text or part of it, without the consent of the author(s) and/or copyright holder(s), unless the work is under an open content license such as Creative Commons.

**Takedown policy**

Please contact us and provide details if you believe this document breaches copyrights. We will remove access to the work immediately and investigate your claim.

# Pareto-Based Modulated Model Predictive Control Strategy for Power Converter Applications

Patricio Santis, Doris Sáez, Roberto Cárdenas and Alfredo Núñez

**Patricio Santis, Doris Sáez and Roberto Cárdenas** are with the Department of Electrical Engineering, University of Chile, Postal Code 8370451, Santiago, Chile.

**Alfredo Núñez** is with the Section of Railway Engineering, Delft University of Technology, Stevinweg 1, 2628 CN Delft, The Netherlands.

*Corresponding Author:* Doris Sáez, Department of Electrical Engineering, University of Chile, email: dsaez@ing.uchile.cl.

## Abstract

Modulated model predictive control ( $M^2PC$ ) allows fixed switching frequency operation of power converters, producing lower ripple and lower total harmonic distortion (THD) in the output signals than those obtained using regular model predictive control (MPC) algorithms. However, the design of the  $M^2PC$  algorithm and its performance depend on, among other factors, the tuning of weighting factors, which are required by the cost functions typically used in predictive control algorithms. In this paper, a novel Pareto-based multi-objective  $M^2PC$  (MO- $M^2PC$ ) strategy is proposed. In this case, the use of weighting factors is not required, and the optimization problem is solved using a multi-objective approach. The aim of the proposed MO- $M^2PC$  strategy is to consider practical rules, such as satisfaction of soft constraints, to calculate the control actions. The proposed Pareto-based MO- $M^2PC$  strategy can be applied to any power converter topology. In this paper, experimental validation of the proposed methodology is pursued using a 3-phase 3 kW power converter operating as a shunt active power filter (SAPF). The proposed control is implemented in a control platform based on the dSPACE ds1103 system. The simulation and experimental results demonstrate the advantages and flexibility achieved by the proposed Pareto-based MO- $M^2PC$ .

25     **Keywords:** Active power filter, model predictive control, modulated model predictive control, multi-  
26 objective optimization, imbalance, harmonic distortion.

27  
28     **I.     Introduction**

29  
30     The applications of power converters have significantly increased in recent years considering the  
31 substantial number of areas where power electronic devices are utilized, such as energy conversion  
32 systems, electric traction, electric drives, and applications related to distributed generation. To convert  
33 energy efficiently and maximize electrical generation, several control strategies have been proposed in the  
34 literature. Among all the proposed strategies, model predictive control (MPC) has been successfully used  
35 for controlling power converters, including explicit control in an optimization framework via a  
36 mathematical model to predict future system behaviour and select appropriate control actions under a  
37 rolling horizon scheme [1] [2] [3] [4].

38     The advantages of MPC include the possibility of designing the objective function with multiple control  
39 objectives and incorporating constraints and nonlinearities into a single control law [1]. Then, some typical  
40 variables in converters, such as current, voltage, power, torque, and flow, among others, can be controlled.  
41 The design of MPC requires, among other issues, the selection of a good set of control objectives in the  
42 cost function. Combining two or more objectives that can sometimes be in opposition to each other into a  
43 single cost function is not a simple task. Traditionally, the mono-objective solution is to linearly combine  
44 each individual objective function using weighting factors, which are used to manage the relative  
45 importance of each term in relation to the other objectives. The tuning of the weighting factors determines  
46 the performance of the controller; however, well-established algorithms for adjusting the weighting factors  
47 are scarce in the literature, and the existing methods are mainly heuristic procedures to estimate these  
48 parameters [5]. In some works, optimization methods, such as the branch and bound algorithm, have been  
49 proposed for selecting the weights; however, because non-convex optimization problems are solved using  
50 these algorithms, the weights may converge into local optimum values. Moreover, to use these methods, the

51 search space must be properly sub-divided to ensure convergence [5] [6].

52 The most common predictive control approach for power converter applications is finite control set MPC  
53 (FCS-MPC) [7] [8] because of its implementation simplicity. However, this technique does not make use of  
54 a modulator to synthesise the voltages; thus, the control can choose only from a limited number of  
55 switching states that are valid at each time instant. This approach generates a relatively large ripple in the  
56 system signals (producing a larger total harmonic distortion (THD)), decreasing the average switching  
57 frequency, thereby decreasing the system performance in terms of the **power quality**. Several strategies  
58 have been proposed in the literature to maintain the switching frequency as fixed or inside a narrow range  
59 (see [9] [10] [11] [12] [13] [14] [15] [16]). For instance, in [15], the fundamental frequency at the output of  
60 the FCS-MPC algorithm is obtained by using a low-pass filter and then synthesised using a modulator  
61 operating at fixed switching frequency. In [16], the frequency spectrum of the currents is shaped by  
62 introducing a band-stop filter in the cost function. However, the application of digital filters has a negative  
63 impact on the dynamic performance of the FCS-MPC algorithm, making this methodology unsuitable for  
64 high-performance applications. In [17], the application of a predictive controller for a 2-level grid-  
65 connected converter is presented. In this case, the converter voltage reference is calculated using a dead-  
66 beat controller, and the gate signals are generated using space vector modulation (SVM) algorithms. A  
67 fixed switching frequency is achieved with this approach, but the implementation of multi-objective control  
68 systems has not been addressed in [17].

69 Recently, modulated MPC ( $M^2PC$ ) has been proposed; this technique contains all the characteristics and  
70 advantages of FCS-MPC and includes a modulation stage, which increases the performance in terms of the  
71 harmonic content of the signal [7] [18] [19] [20] [21]. This technique has been designed for systems that  
72 have a limited number of switching states. Assuming that a given vector has to be synthesised at the  
73 converter output, the duty cycle can be calculated for any state of the converter based on a cost function  
74 that includes the combination of more than one objective. In addition, this technique delivers a fixed  
75 switching frequency for the converter [21], [22]. The  $M^2PC$  strategy has been tested for a lower number of

76 power converter topologies. Among the reported applications of  $M^2PC$  algorithms, both via simulation and  
77 experiments, the following are noteworthy: the seven-level cascaded H-bridge back-to-back converter in  
78 single and three phase [21], a neutral point clamped inverter [23], a two-level inverter [24], an aircraft  
79 generator [25], and active power filters [22] [26].

80 Additionally, some research has been performed based on a multi-objective approach for MPC to avoid  
81 tuning the controller's weighting factors [27] [28] [29]; however, a criterion has to be defined to select the  
82 control action. In [27] and [29], a fuzzy optimization approach is used to obtain the control action of FCS-  
83 MPC without using weighting factors; however, the algorithm depends on the membership function shapes  
84 of the fuzzy sets associated with each objective function. Moreover, a multi-objective predictive control  
85 strategy based on a ranking approach is proposed in [28]. The solution requires some common criteria  
86 among all objective function rankings, and these criteria include the weighting factors of these rankings.

87 In this paper, a novel Pareto-based multi-objective approach for a  $M^2PC$  (MO- $M^2PC$ ) algorithm is  
88 proposed. This strategy includes a different methodology to obtain the control actions instead of the mono-  
89 objective approach typically applied; therefore, the weighting factors are not required. To obtain the control  
90 actions, practical rules are included, such as satisfaction with soft constraints. In this paper, a 3-phase 3 kW  
91 power converter operating as a shunt active power filter (SAPF) is used; however, the proposed Pareto-  
92 based MO- $M^2PC$  strategy can be applied to other power converter topologies. The contributions of this  
93 paper can be summarized as follows:

- 94 • Using the proposed Pareto-based MO- $M^2PC$ , the time-consuming algorithms proposed in the  
95 literature to tune the weighting factors of the cost function are avoided. A methodology based on  
96 the Pareto front is proposed in this work, so that users can visualize the trade-offs between Pareto  
97 optimal solutions.
- 98 • To select a control solution, constraints can be considered, such as the maximum tracking errors  
99 allowed and maximum value of reactive power supplied.
- 100 • Soft constraints can be implemented if required. For instance, if a particular tracking error cannot

101 be achieved, the solution closest to satisfying this requirement can be selected among all the  
102 available solutions.

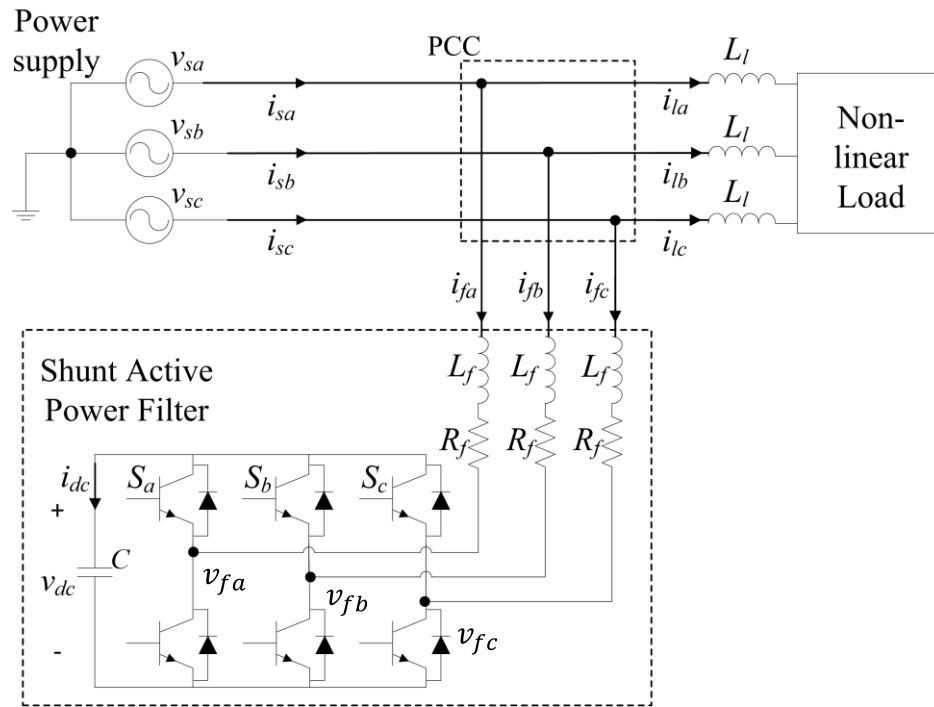
103  
104 The rest of this paper is organized as follows. Section II describes the topology of the active power filter  
105 proposed to validate the control strategies analysed in this work. Section III discusses the M<sup>2</sup>PC technique,  
106 including a new delay compensation method. Section IV introduces the proposed multi-objective  
107 optimization for M<sup>2</sup>PC, using soft constraints as criteria for selecting Pareto optimal solutions. Simulation  
108 and experimental results are presented in Sections V and VI, respectively. Finally, conclusions are  
109 presented in Section VII.

## 111 II. Shunt Active Power Filter Modelling for MPC Design

112 The power converter topology used to validate the proposed Pareto-based MO-M<sup>2</sup>PC is a SAPF [26], as  
113 shown in Fig. 1. In this section, the phenomenological equations of the considered SAPF topology are  
114 described, and these equations are useful for implementing either M<sup>2</sup>PC or MO-M<sup>2</sup>PC.

### 115 A. SAPF Model Description

116 Fig. 1 shows a schematic diagram of an SAPF composed of a two-level 3-wire inverter, where  $v_{dc}$  and  $i_{dc}$   
117 are the voltage and current of the dc-link capacitor, respectively;  $S_i$  is the switching state of the inverter;  $i_{fi}$   
118 is the active power filter current;  $v_{fi}$  is the output voltage of the inverter;  $i_{li}$  is the load current;  $i_{si}$  is the  
119 source current;  $v_{si}$  is the source voltage; and  $i$  is the phase, i.e.,  $i = a, b, c$ .



121

122 Fig. 1. Diagram of a three-phase two-level SAPF.

123 A typical SAPF topology comprises a voltage inverter whose dc-link side is connected to a capacitor  
 124 bank ( $C$  in Fig. 1). Additionally, the AC side is connected to the grid power supply at the point of common  
 125 coupling (PCC) through a first-order power filter, with the filter inductor  $L_f$  and  $R_f$  as the parasitic  
 126 resistance of  $L_f$  (see Fig. 1). In such a configuration, the active filter operates as a controllable current  
 127 source, eliminating the distorted and unbalanced current components from the grid-side current [22].  
 128 Therefore, the SAPF compensates for the unbalanced components, reactive currents, and harmonic currents  
 129 generated under the operation of different types of loads (balanced/unbalanced, linear/non-linear, etc.). The  
 130 inductor loads ( $L_l$ ) are also part of the non-linear loads. A dynamic model of the active power filter is  
 131 presented in [22] [26]. For completeness, this model is briefly discussed in the next section.

132 *B. SAPF Predictive Model for MPC Design*

133 Let us define the following vectors at time  $k$  in the  $\alpha\beta$  reference frame: the output voltage of the inverter  
 134  $\mathbf{v}_f[k]$ , the switching states  $\mathbf{s}[k]$  and the power supply voltage  $\mathbf{v}_s[k]$ . These vectors are shown in Equations  
 135 (1). In the variable definitions, “s” means variables associated with the power supply, and “f” corresponds  
 136 to variables associated with the active power filter (see Fig. 1).

137

$$\mathbf{v}_f[k] \equiv \begin{bmatrix} v_{f\alpha}[k] \\ v_{f\beta}[k] \end{bmatrix}, \mathbf{s}[k] \equiv \begin{bmatrix} s_\alpha[k] \\ s_\beta[k] \end{bmatrix}, \mathbf{v}_s[k] \equiv \begin{bmatrix} v_{s\alpha}[k] \\ v_{s\beta}[k] \end{bmatrix}. \quad (1)$$

138 Moreover, let us assume that the supply (source) currents  $\mathbf{i}_s[k]$ , the load currents  $\mathbf{i}_l[k]$  and the filter  
 139 currents  $\mathbf{i}_f[k]$  are respectively given by the expressions shown in Equations (2) ("l" means variables  
 140 related to the loads; see Fig. 1).

$$\mathbf{i}_s[k] \equiv \begin{bmatrix} i_{s\alpha}[k] \\ i_{s\beta}[k] \end{bmatrix}, \mathbf{i}_l[k] \equiv \begin{bmatrix} i_{l\alpha}[k] \\ i_{l\beta}[k] \end{bmatrix}, \mathbf{i}_f[k] \equiv \begin{bmatrix} i_{f\alpha}[k] \\ i_{f\beta}[k] \end{bmatrix}. \quad (2)$$

141 To obtain the dynamic equations of the SAPF, a Kirchoff analysis is used as follows:

$$\begin{aligned} & \text{---} \\ & \text{---} \end{aligned} \quad (3)$$

142 where  $\text{---}$  is the inductance voltage of the filter for  $\beta$ ;  $\text{---}$  is the filter resistance  
 143 voltage for  $\beta$ ; and  $\text{---}$  is the dc-link current.

144 From the previous expressions, a state representation of the SAPF in the continuous time domain is  
 145 obtained as follows:

$$\begin{aligned} & \text{---} \\ & \text{---} \\ & \text{---} \end{aligned} \quad (4)$$

146

147 The Euler approximation is used to obtain a discrete model system with sampling time  $T_s$ .

$$\begin{aligned} & \text{---} \\ & \text{---} \\ & \text{---} \end{aligned} \quad (5)$$

148



149 Thus, the state vector at the instant time  $k$  is given by:  $\mathbf{x}[k] = [\mathbf{i}_f[k]^T \ v_{dc}[k]]^T = [i_{f\alpha}[k] \ i_{f\beta}[k] \ v_{dc}[k]]^T$ .

150 Based on that vector, the equation system shown in (5) is given in matrix format in Equation (6). To

151 implement the MPC strategies, the following model in Equation (6) is used (see [22]):

$$\hat{\mathbf{x}}[k+1] = f(\mathbf{x}[k], \mathbf{s}[k], \mathbf{v}_s[k], T_s) = \begin{bmatrix} \left(1 - \frac{R_f T_s}{L_f}\right) \mathbf{I}_{2 \times 2} & -\frac{T_s}{L_f} \mathbf{s}[k] \\ \frac{T_s}{C} (\mathbf{s}[k])^T & 1 \end{bmatrix} \mathbf{x}[k] + \begin{bmatrix} \frac{T_s}{L_f} \mathbf{I} \\ \mathbf{0}_{1 \times 2} \end{bmatrix} \mathbf{v}_s[k], \quad (6)$$

152 where  $\mathbf{0}$  is a vector with zeros, and  $\mathbf{I}$  is an identity matrix.

153 The power supply currents are as follows:

$$\mathbf{i}_s[k] = \mathbf{i}_l[k] + \mathbf{i}_f[k]. \quad (7)$$

154 Using Equation (7), it is possible to predict the relevant control variables for the SAPF system, i.e., the

155 active and reactive power supplied by the source,  $\hat{P}_s$  and  $\hat{Q}_s$ , respectively,

$$\hat{P}_s[k+1] = (\mathbf{i}_s[k+1])^T \begin{bmatrix} 1 & 0 \\ 0 & 1 \end{bmatrix} \mathbf{v}_s[k+1], \quad (8)$$

$$\hat{Q}_s[k+1] = (\mathbf{i}_s[k+1])^T \begin{bmatrix} 0 & -1 \\ 1 & 0 \end{bmatrix} \mathbf{v}_s[k+1].$$

156 Then, the references for the active and reactive power  $P_s^*$  and  $Q_s^*$  are computed. The reference  $Q_s^*$  is

157 assumed to be known, and in this paper, this reference is considered to be zero. The reference  $P_s^*$  is

158 calculated as follows (based on [30]):

$$\mathbf{P}_l^* \quad (9)$$

159 where  $P_l^*$  is the power load reference and  $P_f^*$  is the power filter reference.  $P_l^*$  is the dc component given

160 by:

$$P_l^*[k+1] = (\mathbf{i}_l[k+1])^T \mathbf{v}_s[k+1]. \quad (10)$$

161 If power oscillations produced by unbalanced or distorted signals are present in Equation (10), then a

162 simple discretised second-order Butterworth filter, with a cut-off frequency of 25 Hz, can be applied to  $P_s^*$ .

163 The vector  $\mathbf{i}_l[k+1]$  is obtained by a linear prediction [8]. This approach means that the current is predicted

164 by considering two steps ahead. Based on that approach, if the sampling time is small compared to the load  
 165 dynamics, the following linear predictor is used:  $i_l[k+2]=1.5i_l[k]-0.5i_l[k-1]$  (see [8]). The power supply  
 166 voltage vector  $v_s[k+1]$  is obtained using the following linear extrapolation:  $v_s[k+2]=2v_s[k+1]-v_s[k]$  (see  
 167 [31]). This extrapolation can be used since the switching frequency used in this paper is high, such that  
 168  $kHz$ .

169 The power required to regulate the dc-link reference  $P_{dc}^*$  is obtained as follows:

$$P_{dc}^*[k+1]=\tilde{v}_{dc}^*[k+1]i_{dc}^*[k+1]. \quad (11)$$

170 where  $\tilde{v}_{dc}^*$  is the filtered reference dc voltage and  $i_{dc}^*$  is the reference dc current. The dynamic of the dc-  
 171 link voltage is typically slower than that of the AC-side active power. The prediction horizon reference  $N$  is  
 172 introduced to calculate the filtered voltage  $\tilde{v}_{dc}^*[k+1]$  [30]. This voltage is obtained by using the measured  
 173 dc-link voltage  $v_{dc}[k]$  at time  $k$  as follows:

$$\tilde{v}_{dc}^*[k+1]=v_{dc}[k]+\frac{1}{N}(v_{dc}^*[k]-v_{dc}[k]) \quad (12)$$

174 where the reference voltage is  $v_{dc}^*[k]$ , and the variable  $N$  allows the converter to reach the reference  
 175 voltage  $v_{dc}^*[k]$  linearly in  $N$  samples.

176 Furthermore, the reference current  $i_{dc}^*$  required for the filtering voltage is given by:

$$i_{dc}^*[k+1]=\frac{C}{T_s N}(v_{dc}^*[k]-v_{dc}[k]). \quad (13)$$

177 Thus, the current in the capacitor is limited to  $(100/N)\%$  of the current required for the voltage  $v_{dc}$  to  
 178 reach the reference voltage  $v_{dc}^*$  in one sampling period.

179

### 180 III. Modulated model predictive control

181 M<sup>2</sup>PC is based on a conventional predictive control scheme embedded with a SVM algorithm [22] [24].  
 182 For a two-level inverter, the implementation of the SVM algorithm requires the calculation of three duty  
 183 cycles [22] [24]. For M<sup>2</sup>PC, the duty cycles are calculated using a cost function, which can be composed of

184 several objectives. For a two-level voltage source power converter, there are six valid active vectors and  
 185 two zero vectors. Table I shows the vectors **in the abc frame** and the corresponding phase-to-neutral  
 186 voltages generated by these vectors. Note that the zero vectors are  $\mathbf{v}_0$  and  $\mathbf{v}_7$ .

187 TABLE I: Phase-phase voltage inverter output for two levels

	$\mathbf{v}_0$	$\mathbf{v}_1$	$\mathbf{v}_2$	$\mathbf{v}_3$	$\mathbf{v}_4$	$\mathbf{v}_5$	$\mathbf{v}_6$	$\mathbf{v}_7$
$v_{fab}[k]$	0	$v_{dc}$	0	$-v_{dc}$	$-v_{dc}$	0	$v_{dc}$	0
$v_{fbc}[k]$	0	0	$v_{dc}$	$v_{dc}$	0	$-v_{dc}$	$-v_{dc}$	0
$v_{fac}[k]$	0	$-v_{dc}$	$-v_{dc}$	0	$v_{dc}$	$v_{dc}$	0	0

188

189 In this paper, the SVM algorithm is implemented using the six modulation sectors typically used for 2-  
 190 level power converters. Sector 1 is composed of vectors  $\mathbf{v}_0$ ,  $\mathbf{v}_1$ ,  $\mathbf{v}_2$ , sector 2 of vectors  $\mathbf{v}_0$ ,  $\mathbf{v}_2$ ,  $\mathbf{v}_3$ , sector 3 of  
 191 vectors  $\mathbf{v}_0$ ,  $\mathbf{v}_3$ ,  $\mathbf{v}_4$ , sector 4 of vectors  $\mathbf{v}_0$ ,  $\mathbf{v}_4$ ,  $\mathbf{v}_5$ , sector 5 of vectors  $\mathbf{v}_0$ ,  $\mathbf{v}_5$ ,  $\mathbf{v}_6$  and sector 6 of vectors  $\mathbf{v}_0$ ,  $\mathbf{v}_6$ ,  $\mathbf{v}_1$ .

192 To implement  $M^2PC$ , it is necessary to consider the delay of the actuator, i.e., the inverter. **Therefore, the**  
 193 **predicted values of the state variables ( $\hat{\mathbf{x}}[k+1]$ ) required to compensate for this delay are obtained by**  
 194 **using the method proposed in [32] but considering the symmetrical switching pattern that reduces the**  
 195 **current ripple [7]. Based on that method, seven equations are obtained, one for each switching state, as**  
 196 **shown in Equations (14).**

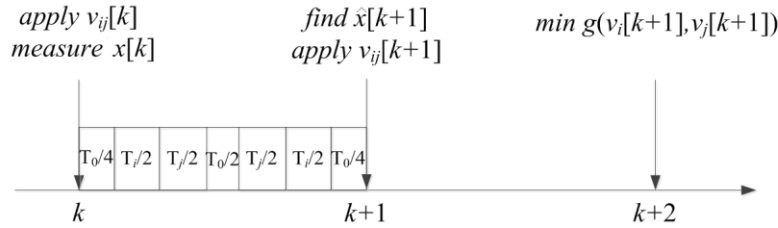
$$\begin{aligned}
 \hat{\mathbf{x}}[k+T_s^0, k] &= f(\mathbf{x}[k], \mathbf{s}[k], \mathbf{v}_{ij}[t, k], T_s^0) \\
 \hat{\mathbf{x}}[k+T_s^\ell, k] &= f(\hat{\mathbf{x}}[k+T_s^{\ell-1}, k], \mathbf{s}[k], \mathbf{v}_{ij}[k+T_s^{\ell-1}, k], \Delta T_s^\ell), \quad \ell = 1, \dots, 5 \\
 \hat{\mathbf{x}}[k+T_s, k] &= \hat{\mathbf{x}}[k+1] = f(\hat{\mathbf{x}}[k+T_s^5, k], \mathbf{s}[k], \mathbf{v}_{ij}[k+T_s^5, k], T_s - T_s^5)
 \end{aligned} \tag{14}$$

197 where  $\hat{\mathbf{x}}[k+T_s^\ell, k]$  is **the state equation in instant** ,  $\hat{\mathbf{x}}[k+1]$  is the state in instant **1**, function  
 198  $f(\cdot, \cdot, \cdot, \cdot)$  is given by Equation (6),  $\mathbf{v}_{ij}[t, k]$  are the voltages for each sector,  $\Delta T_s^\ell = T_s^\ell - T_s^{\ell-1}$ ,  $T_s^0 = T_0/4$ ,  
 199  $T_s^1 = T_s^0 + T_i/2$ ,  $T_s^2 = T_s^1 + T_j/2$ ,  $T_s^3 = T_s^2 + T_0/2$ ,  $T_s^4 = T_s^3 + T_j/2$ , and  $T_s^5 = T_s^4 + T_i/2$ ;  $T_0$ ,  $T_i$  and  $T_j$  are **the duty**  
 200 **cycles for the voltage vectors  $v_0$ , and , respectively.**

201

202 It is important to highlight that Equations (14) are required to compensate for the delay of one sampling  
 203 time imposed by the 2-level inverter. Therefore,  $\hat{\mathbf{x}}[k+1]$  represents an estimation of the states in  $k+1$   
 204 considering the control action applied in the  $k$ -th sampling time. Fig. 2 shows a delay compensation scheme

205 for M2PC. A prediction is performed at each sampling time to obtain the corresponding control action.



206  
207 Fig. 2. Delay compensation for M<sup>2</sup>PC.

208 Using  $\hat{x}[k+1]$  obtained in Equations

209 (14) as the initial condition, the predictions  $\hat{x}[k+2]$  (for all the valid states) are obtained by solving

210  $\hat{x}[k+2] = f(\hat{x}[k+1], s[k+1], \mathbf{v}_{ij}[k+1], T_s)$ . Therefore, considering the explained delay compensation and using

211 the active and reactive power supplied by the power supply as presented in Equations (8) and (9), the

212 following cost function  $G$  is defined for the active power filter voltage vectors  $\mathbf{v}_i$ ,  $i = 0, \dots, 6$ :

$$G(\mathbf{v}_i[k+1]) = \left( \hat{P}_s[k+2] \Big|_{\mathbf{v}_i[k+1]} - P_s^*[k+2] \right)^2 + \lambda \left( \hat{Q}_s[k+2] \Big|_{\mathbf{v}_i[k+1]} - Q_s^*[k+2] \right)^2 \quad (15)$$

213 where  $\hat{P}_s[k+2] \Big|_{\mathbf{v}_i[k+1]}$  and  $\hat{Q}_s[k+2] \Big|_{\mathbf{v}_i[k+1]}$  are the active and reactive power supplied by the source and are

214 calculated as in Equation (8) for instant  $k+1$ . Note that Equation (15) is used for the conventional M2PC

215 formulation, where a weighting factor  $\lambda$  is still required. In Section IV, a Pareto-based algorithm is

216 proposed to eliminate the need to define weighting factors.

217 Consider the cost functions  $G_0$ ,  $G_i$  and  $G_j$  defined as follows:  $G_0[k+2] = G(\mathbf{v}_0[k+1])$ ,

218  $G_i[k+2] = G(\mathbf{v}_i[k+1])$ , and  $G_j[k+2] = G(\mathbf{v}_j[k+1])$ . The cost functions  $G_0[k+2]$ ,  $G_i[k+2]$ , and  $G_j[k+2]$

219 are related to the zero vector  $\mathbf{v}_0$  and the active vectors  $\mathbf{v}_i$ ,  $\mathbf{v}_j$ , respectively, with  $(i, j) \in \{(1,2), (2,3), (3,4),$

220  $(4,5), (5,6), (6,1)\}$ , according to Table I; the SVM modulation computes the cycle times  $(d_0, d_i$  and  $d_j)$  of

221 the active and zero vectors by solving the following:

$$d_0 = \frac{D}{G_0[k+2]}, d_i = \frac{D}{G_i[k+2]}, d_j = \frac{D}{G_j[k+2]}, d_0 + d_i + d_j = 1, \quad (16)$$

222 where  $D$  is a constant required in Equations (16) to achieve  $d_0 + d_i + d_j = 1$  (this constant is derived below;

223 see Equation (19)). The duty cycle of the zero vector corresponds to  $d_0$  and is applied in total during

224  $T_0 = T_s d_0$ , where  $T_s$  is the sampling time. The duty cycles for the active vectors  $\mathbf{v}_i$  and  $\mathbf{v}_j$  are  $d_i$  and  $d_j$  and  
 225 are applied during  $T_i = T_s d_i$  and  $T_j = T_s d_j$ , respectively.

226 For M<sup>2</sup>PC, the following cost function, comprising the effects of the two applied active vectors  $\mathbf{v}_i$  and  $\mathbf{v}_j$ ,  
 227 is optimized [24]:

$$g(\mathbf{v}_i[k+1], \mathbf{v}_j[k+1]) = d_0 G_0[k+2] + d_i G_i[k+2] + d_j G_j[k+2] \quad (17)$$

228  
 229 Substituting Equations (16) into Equation (17), the cost function is rewritten as:

$$g(\mathbf{v}_i[k+1], \mathbf{v}_j[k+1]) = \frac{DG_0[k+2]}{G_0[k+2]} + \frac{DG_i[k+2]}{G_i[k+2]} + \frac{DG_j[k+2]}{G_j[k+2]} = 3D \quad (18)$$

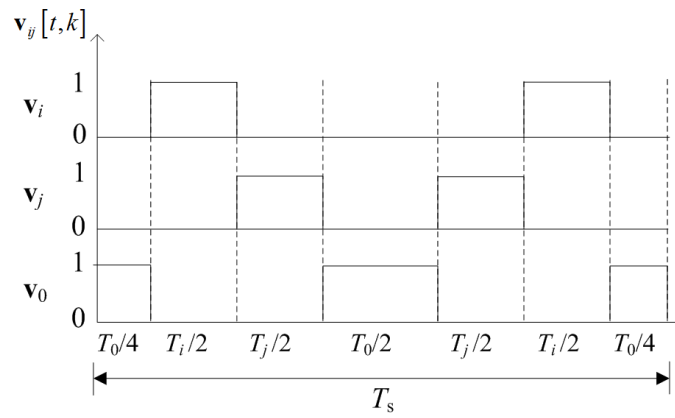
230 We use the constraint  $d_0 + d_i + d_j = 1$  to obtain  $D$  as follows:  
 231

$$D = \frac{G_i[k+2]G_j[k+2]G_0[k+2]}{G_i[k+2]G_0[k+2] + G_i[k+2]G_j[k+2] + G_j[k+2]G_0[k+2]} \quad (19)$$

232  
 233 The two active vectors that minimize this new cost function are selected and applied to the converter in  
 234 the next instant of time  $k+1$ . After obtaining the duty cycles and selecting the optimal active vectors, a  
 235 symmetrical switching pattern is adopted to reduce the signal ripple (see Fig. 3 for an example). Equation  
 236 (20) is a continuous function over  $t$ , defined at every decision instant time  $k$  (during sampling time  $T_s$ ), and  
 237 this equation is applied once the decision-making process determines the active vectors  $\mathbf{v}_i$  and  $\mathbf{v}_j$  and  
 238 their applied times  $T_i$  and  $T_j$  (which are the duty cycles  $d_i$  and  $d_j$  multiplied by the sampling time),  
 239 respectively. At the beginning, middle and end of the cycle, the vector  $\mathbf{v}_0$  is applied according to the  
 240 calculated duty cycle  $d_0$  in total during  $T_0$ . Equation (20) captures a symmetrical pattern for M<sup>2</sup>PC to reduce  
 241 the signal ripple [23].  
 242

$$\mathbf{v}_{ij}[t, k] = \begin{cases} \mathbf{v}_0 & \text{if } t \in [k, k+T_s^0) \cup [k+T_s^2, k+T_s^3) \cup [k+T_s^5, k+T_s) \\ \mathbf{v}_i & \text{if } t \in [k+T_s^1, k+T_s^4) \cup [k+T_s^4, k+T_s^5) \\ \mathbf{v}_j & \text{if } t \in [k+T_s^1, k+T_s^2) \cup [k+T_s^3, k+T_s^4) \end{cases} \quad (20)$$

243 where  $T_s^0 = T_0/4$ ,  $T_s^1 = T_s^0 + T_i/2$ ,  $T_s^2 = T_s^1 + T_j/2$ ,  $T_s^3 = T_s^2 + T_0/2$ ,  $T_s^4 = T_s^3 + T_j/2$ , and  $T_s^5 = T_s^4 + T_i/2$ .  
 244



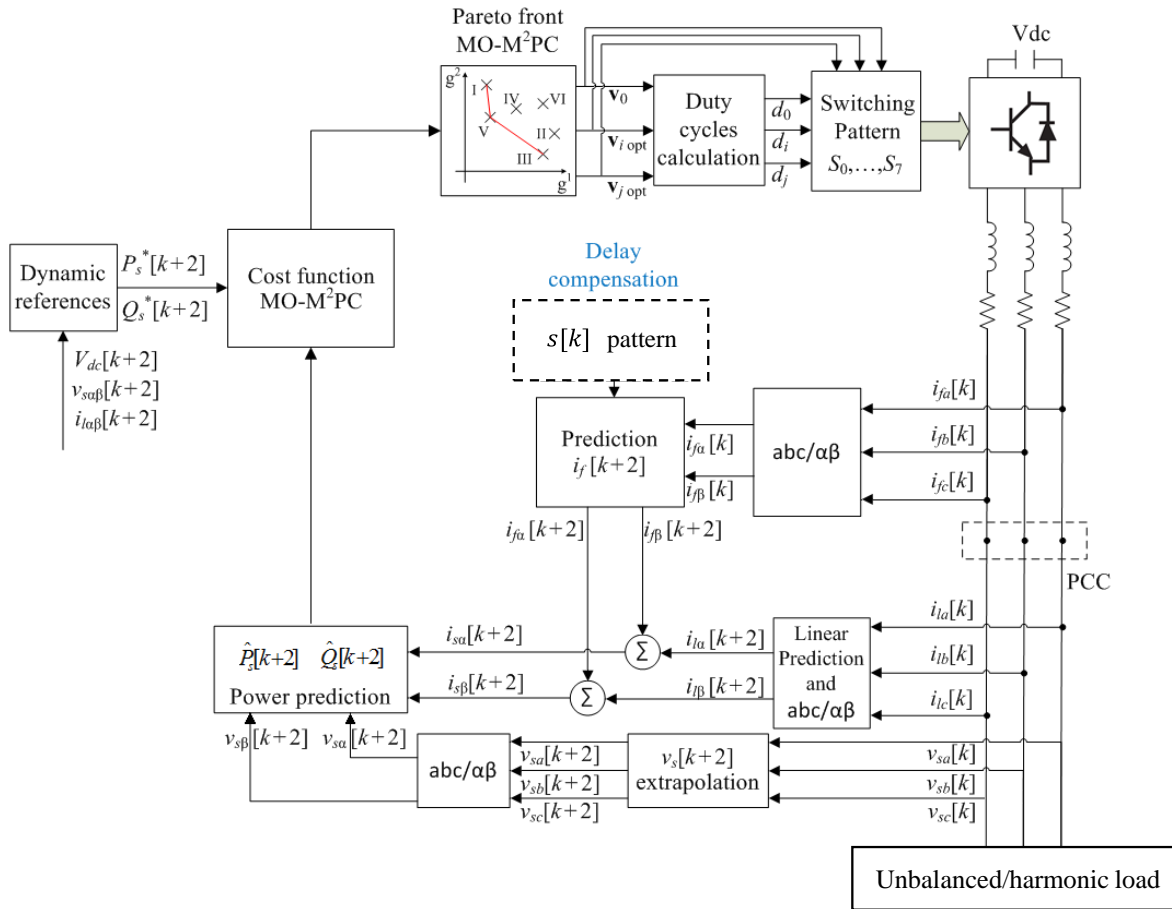
245

246 Fig. 3. Symmetrical pattern for M<sup>2</sup>PC [23].

247 **IV. Design of Pareto-based MO-M<sup>2</sup>PC**

248 The proposed control scheme is depicted in Fig. 4. It worth remembering that the proposed scheme is  
 249 developed for an active power filter in shunt connection. In this figure, all the steps necessary to implement  
 250 the proposal are shown. These steps are discussed in this section.

251



252

253 Fig. 4. Scheme of the proposed control system.

254

255 The optimal selection of the weighting factors of the cost function in an MPC strategy is an open issue in  
 256 general, including the case of power converters. Heuristics are the most commonly used methodologies.  
 257 MO-M<sup>2</sup>PC is a generalization of M<sup>2</sup>PC that can be designed to facilitate the design of the controller and  
 258 associated cost function, i.e., avoiding the tuning of the weighting factors. In general, a multi-objective  
 259 optimization problem minimizes a set of objective functions as follows:

$$\min_{s[k] \in \mathbb{S}^2} \mathbf{g}[k] = \left[ g^1(s[k]), g^2(s[k]), \dots, g^m(s[k]) \right]^T \quad (21)$$

260 where  $\{g^p(s[k])\}_{p=1, \dots, m}$  corresponds to the “ $p$ ” normalized cost functions of the system (or, in per unit),  
 261 with  $p=1, \dots, m$ , where  $m$  corresponds to the number of cost functions within the objective function;  $s[k]$  is  
 262 the vector of the decision variables; and  $\mathbb{S}^2$  is the set of valid states. The solution of an MO-M<sup>2</sup>PC problem  
 263 is a set of Pareto optimal solutions. A solution  $s_q[k] \in \mathbb{S}^2$ , where  $q \in \{1, \dots, m\}$ , is Pareto optimal if [28]:

$$\nexists_q s[k] \in \mathbb{S}^2 : \forall h, g^h(s_q[k]) \leq g^h(s_p[k]) \wedge \exists j : g^j(s_q[k]) < g^j(s_p[k]), \quad (22)$$

264 where  $p, q \in \{1, \dots, m\}$ ,  $p \neq q$ , and  $\mathbb{S}^2$  is the set of valid states. In this case, each  $s_q[k] \in \mathbb{S}^2$  represents a sector,  
 265 i.e., a pair of adjacent vectors.

267 In general, the Pareto frontier can comprise many feasible solutions. In this case, a criterion must be  
 268 used to select the pair of adjacent vectors among all the possibilities within the Pareto optimal set. To  
 269 facilitate decision making, the Pareto set is evaluated in the objective function space to generate the so-  
 270 called Pareto optimal front.

271 Assuming that the objective functions are normalized, a possible criterion can consider selecting the  
 272 solution in the Pareto front that is closest to the origin so that the tuning parameter becomes an easily  
 273 interpreted variable, such as meeting certain constraints  $g^i(s[k]) \leq \epsilon_i$ ,  $i=1, 2, \dots, m$ . If the problem  
 274 becomes unfeasible due to the constraints, the solution within the Pareto set that is closest to the feasible set  
 275 can be adopted as a form of soft constraint. To illustrate the proposed MO-M<sup>2</sup>PC scheme, the case of two

276 objectives is shown for the 2-level inverter, i.e., with six valid active sectors. We first define the following  
 277 vector of functions:

$$G_{\text{MO-M}^2\text{PC}}(\mathbf{v}_i[k+1]) = \begin{pmatrix} \left( \hat{P}_s[k+2] \Big|_{\mathbf{v}_i[k+1]} - P_s^*[k+2] \right)^2 \\ \left( \hat{Q}_s[k+2] \Big|_{\mathbf{v}_i[k+1]} - Q_s^*[k+2] \right)^2 \end{pmatrix} = \begin{pmatrix} G_{\text{MO-M}^2\text{PC}}^1(\mathbf{v}_i[k+1]) \\ G_{\text{MO-M}^2\text{PC}}^2(\mathbf{v}_i[k+1]) \end{pmatrix} = \begin{pmatrix} G_i^1[k+2] \\ G_i^2[k+2] \end{pmatrix} \quad (23)$$

278 Similarly, by evaluating  $\mathbf{v}_0[k+1]$  or  $\mathbf{v}_j[k+1]$  in Equation (23), we obtain  $G_0^1[k+2]$  and  $G_0^2[k+2]$  (when  
 279 evaluating  $\mathbf{v}_0[k+1]$ ) and  $G_j^1[k+2]$  and  $G_j^2[k+2]$  (when evaluating  $\mathbf{v}_j[k+1]$ ). To calculate the duty cycles of  
 280 the selected vectors, these duty cycles are considered to be inversely proportional to the Euclidean distance  
 281 of the cost functions as follows:

$$d_0 = \frac{D_{\text{MO-M}^2\text{PC}}}{\sqrt{G_0^1[k+2] + G_0^2[k+2]}}, d_i = \frac{D_{\text{MO-M}^2\text{PC}}}{\sqrt{G_i^1[k+2] + G_i^2[k+2]}}, d_j = \frac{D_{\text{MO-M}^2\text{PC}}}{\sqrt{G_j^1[k+2] + G_j^2[k+2]}}, d_0 + d_i + d_j = 1 \quad (24)$$

282 where  $D_{\text{MO-M}^2\text{PC}}$  is a constant that guarantees that the sum of the cycles is equal to one. Then, the multi-  
 283 objective cost function to be optimized is the following:

$$\mathbf{g}(\mathbf{v}_i[k+1], \mathbf{v}_j[k+1]) = \begin{pmatrix} d_0 G_0^1[k+2] + d_i G_i^1[k+2] + d_j G_j^1[k+2] \\ d_0 G_0^2[k+2] + d_i G_i^2[k+2] + d_j G_j^2[k+2] \end{pmatrix} = \begin{pmatrix} g^1(\mathbf{v}_i[k+1], \mathbf{v}_j[k+1]) \\ g^2(\mathbf{v}_i[k+1], \mathbf{v}_j[k+1]) \end{pmatrix} \quad (25)$$

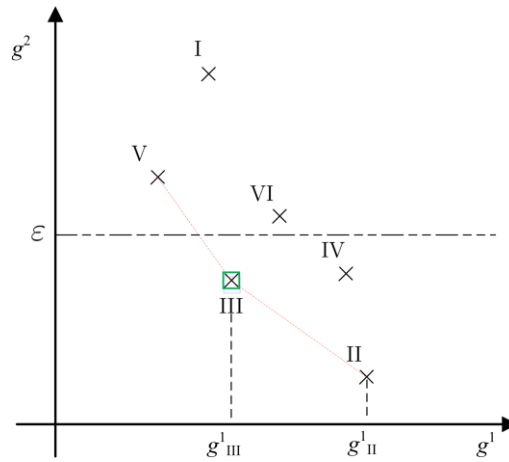
284 Finally, the Pareto front of the two active vectors is obtained. From this front, the vectors are selected  
 285 based on pre-established criteria and applied to the converter in the next time instant  $k+1$ . After obtaining  
 286 the duty cycles and selecting the optimal active vectors, the same symmetrical switching pattern discussed  
 287 in Section III is used.

289 One criterion corresponds to solving the multi-objective problem of determining the point belonging to  
 290 the Pareto front that is closest to the origin and satisfies  $g^2(\mathbf{v}_i[k+1], \mathbf{v}_j[k+1]) \leq \varepsilon$ , where  $\varepsilon$  is a constant that  
 291 limits the value of  $g^2(\mathbf{v}_i[k+1], \mathbf{v}_j[k+1])$ . This criterion is known as the "epsilon constraint" in the literature.  
 292 It should be pointed out that this latter expression is related to the reactive power; therefore, only a  
 293 restriction on the reactive power is considered in this paper (constraints on  $g^1(\mathbf{v}_i[k+1], \mathbf{v}_j[k+1])$  could be  
 294 considered as well; however, in this work, these constraints are not studied). Fig. 5 shows an example of  
 295 Pareto conditions for MO-M<sup>2</sup>PC. In this figure, I, II, III, IV, V, and VI correspond to the sectors of the



296 **SVM algorithm.** For the example depicted in Fig. 5, the possible solutions to the problem are sectors II, III  
297 and IV. Immediately, sector IV is discarded because it does not belong to the Pareto frontier. The optimum  
298 of the problem is sector III because the condition for  $g^2$  is fulfilled, and this sector is the closest-to-the-  
299 origin state.

300 Finally, the proposed MO-M<sup>2</sup>PC method is summarized in the flow chart in Fig. 6.



301

302 Fig. 5. Example Pareto condition for MO-M<sup>2</sup>PC.

303

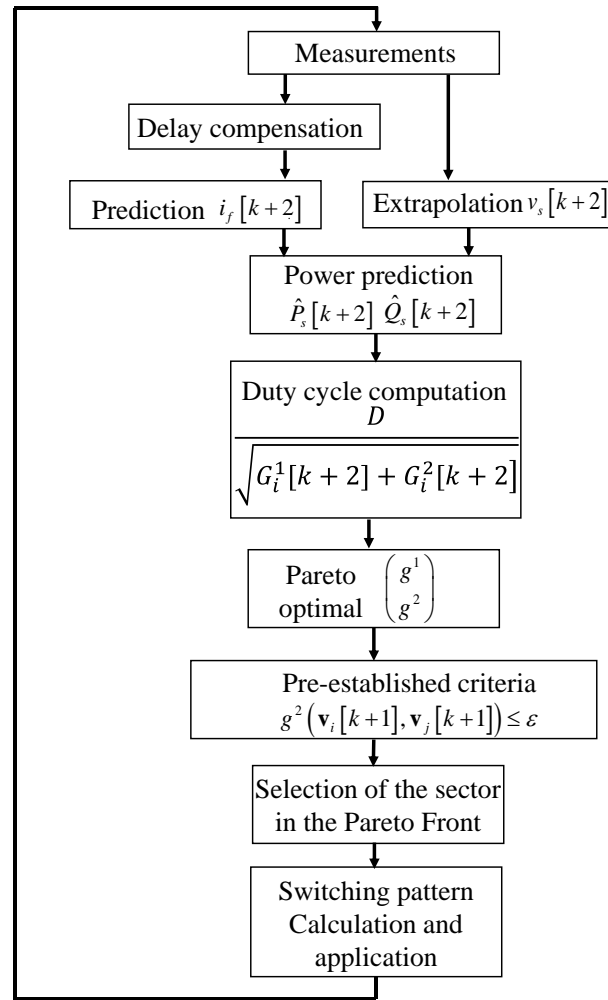


Fig. 6. Flow chart of the MO-M<sup>2</sup>PC algorithm.

## V. Simulation Results

Using a simulation model implemented in MATLAB/SIMULINK software, the performance of the Pareto-based multi-objective control system (see Fig. 4 and Fig. 6) was evaluated. For the simulation work, the following parameters were used: source voltage AC 85 [Vrms], 50 [Hz]; dc-link voltage 400 [V]; filter inductances of 5 [mH]; filter load of 2.5 [mH]; sampling frequency 10 [kHz]; and a time step of 0.5 [ $\mu$ s].

To validate the proposed multi-objective predictive control strategy, several tests are performed using different optimization criteria to select the sector with the three vectors required to synthesise the output voltage. In the first of these tests, the solution sector is obtained by identifying the closest point to the origin within the optimal Pareto front in Equation

317 (25) (see Fig. 5). The other criterion corresponds to a constraint on the reactive power error  $|e_Q| = |Q_s -$   
318  $Q_s^*|$ , where  $Q_s$  is the power supply-side reactive power calculated using Equation (8) and  $Q_s^*$  is the  
319 reference, which in this case is equal to zero. This constraint is defined as  $|e_Q| < e_{Q_{\max}}$ , with  $e_{Q_{\max}}$  values of  
320 200, 100 and 50 [VAR].

321 To evaluate the effectiveness of the proposed MO-M<sup>2</sup>PC, simulation tests were performed for two  
322 disturbance scenarios: connection of an unbalanced linear load and connection of a non-linear balanced  
323 load.

#### 324 A. Unbalanced Linear Load

325 To verify the performance of the proposed control system to compensate for unbalanced loads using the  
326 active power filter shown in Fig. 1, unbalanced 3-wire resistive star-connected loads of 17.5  $\Omega$ , 14  $\Omega$  and 8  
327  $\Omega$  (per phase) were used in the simulation model. The currents produced by these loads are shown in Fig. 7.

328 The simulation results for this test show that the application of the closest-to-the-origin criterion (see Fig.  
329 8(a)) in the Pareto-based algorithm produces current waveforms (at the power supply side) with low THD.  
330 The frequency spectrum corresponding to the waveforms shown in Fig. 8(a) is shown in Fig. 8(e). Note that  
331 most of the harmonics are concentrated in the high-frequency region ( $n=200$ ) corresponding to the side  
332 bands produced by the switching frequency ( $f_s=10$  kHz).

333 As the error band  $Q$  decreases, the distortion in the waveforms increases (see Fig. 8(b)-(d)). This  
334 distortion is produced because, for a smaller error band, there are fewer switching states that can be applied  
335 (see Fig. 5). Moreover, the states selected within the Pareto front are not necessarily optimal considering  
336 the near-to-the-origin criterion. If the error band is large, as shown in Fig. 8(b), the waveforms produced at  
337 the power supply currents are similar to those shown in Fig. 8(a). This result occurs because, for a large  
338 error band, the closest-to-the-origin switching state shown in Fig. 5 can be selected. Finally, Table II  
339 presents the results for the three different multi-objective optimization criteria studied in this work. In this  
340 table, the THD of the supply currents before and after the activation of the active power filter is provided.

341 Fig. 9 shows the currents supplied by the active power filter, corresponding to the tests in Fig. 8(a)-(d).  
 342 The waveforms shown in Fig. 9 corroborate that the currents are more distorted when the error bands for  
 343 the reactive power are smaller. This finding can be appreciated in Fig. 9(d), where there is more distortion  
 344 for the case  $|e_Q| < 50$  [VAR] than for the others cases depicted in Fig. 9.

345 Fig. 10 shows the reactive power injected by the SAPF, considering the different Pareto conditions. As  
 346 depicted in these graphs, there are some operating points where the criteria are not completely fulfilled  
 347 (e.g.,  $|e_Q| < 50$  [VAR]). In this case, the multi-objective problem is solved using "soft constraints" by a  
 348 solution that does not fulfil the constraints but is the best case achieved considering all the available  
 349 solutions.

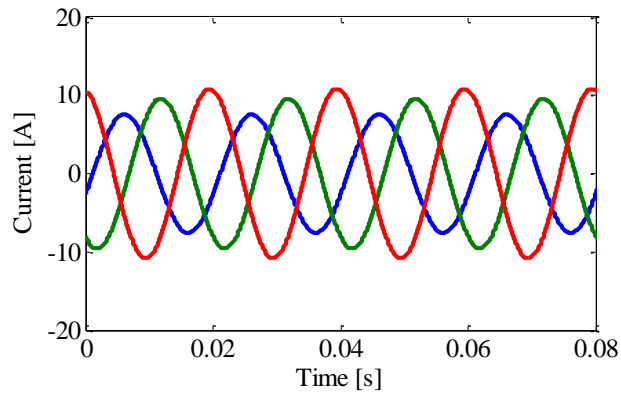
350 Table II shows the values of the fundamental current before and after connecting the SAPF. Initially,  
 351 relatively large unbalanced currents are observed, with imbalances close to 20% between the amplitudes of  
 352 the fundamental currents in different phases. After compensation, the current is well balanced with an  
 353 average difference of 2% between the current amplitudes of different phases.

354

355 TABLE II: **Fundamental current for an unbalanced load before and after connecting the SAPF**

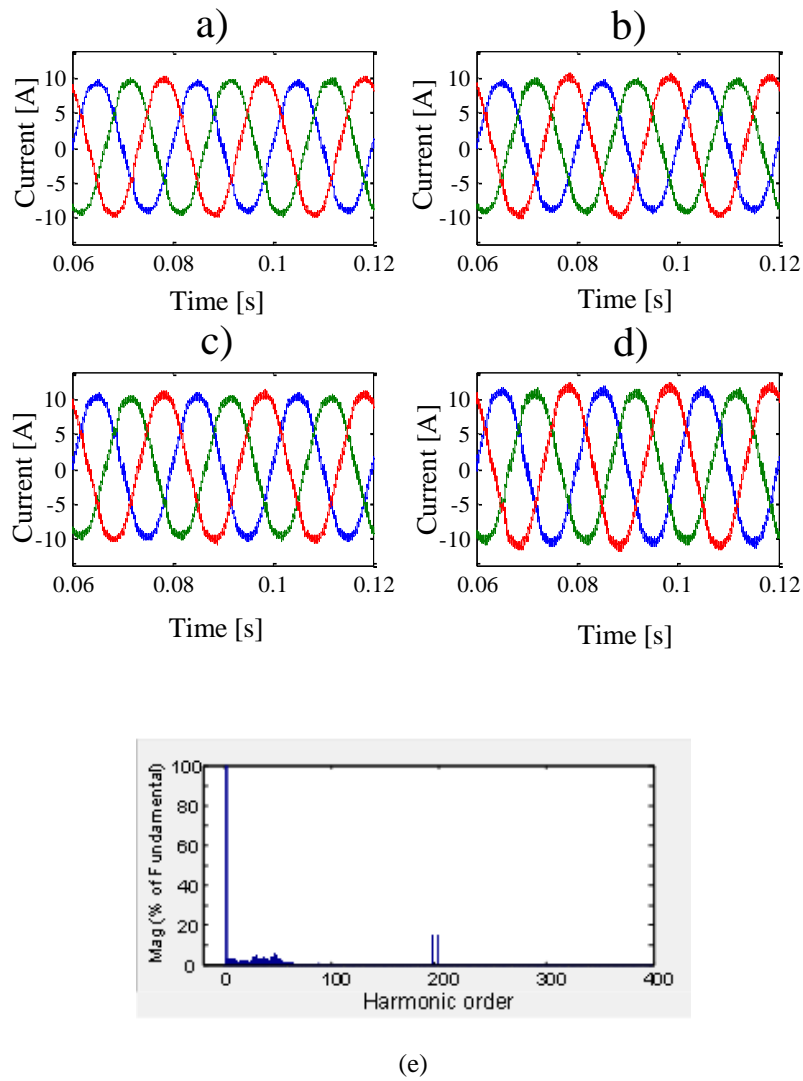
		Near origin	$ e_Q  < 200$ [VAR]	$ e_Q  < 100$ [VAR]	$ e_Q  < 50$ [VAR]
Phase	$I_{fund}$ [A]	$I_{fund}$ [A]			
	Before SAPF	After connecting SAPF			
<i>a</i>	5.34	5.42	5.63	5.93	6.77
<i>b</i>	6.76	5.53	5.72	5.94	6.61
<i>c</i>	7.66	5.68	5.78	6.00	6.83

356



357

358 Fig. 7. Unbalanced load current profile used for simulation purposes.



359

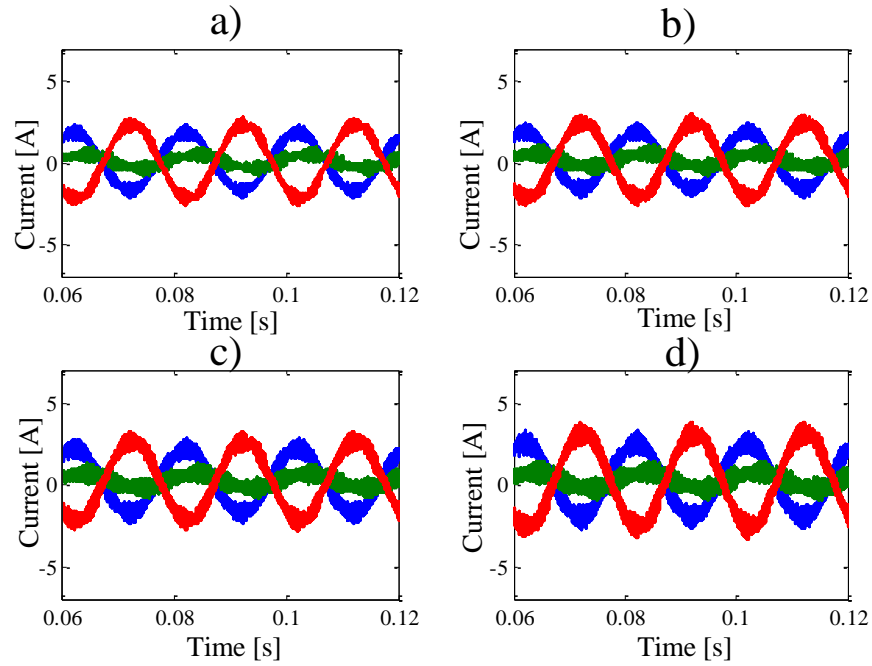
360

361

362

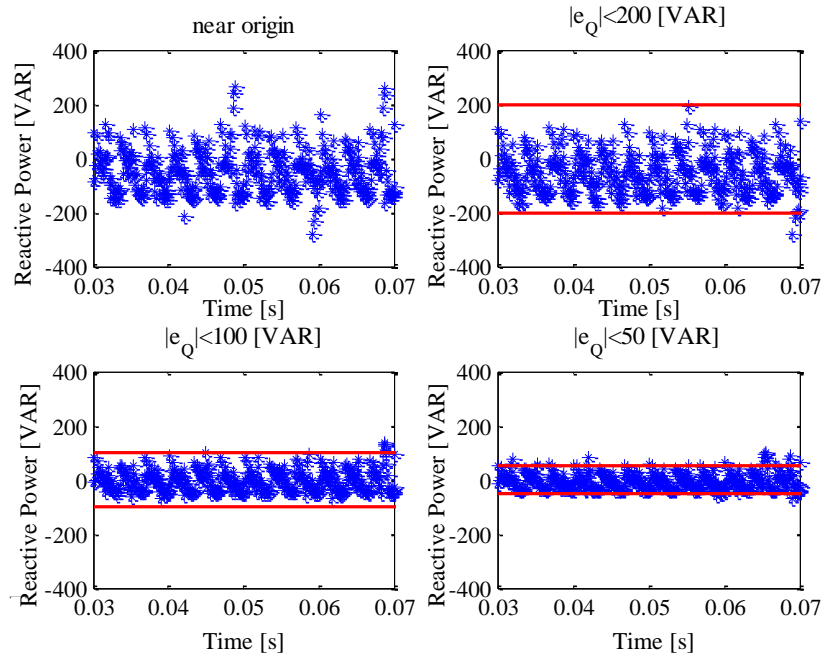
363 Fig. 8. Performance of the currents in the power supply for the proposed control system for an unbalanced load: a) near-origin criterion; b)  $|eQ| < 200$  [VAR]; c)  $|eQ| < 100$  [VAR]; d)  $|eQ| < 50$  [VAR]; e) frequency spectrum corresponding to the waveforms shown in Fig. 8(a).

365



366 Fig. 9. Currents supplied by the SAPF considering the unbalanced load profile shown in Fig. 7. a) Near-origin criterion; b)  $|e_Q| < 200$  [VAR]; c)  $|e_Q| < 100$  [VAR]; d)  $|e_Q| < 50$  [VAR].  
 367  
 368

369



370

371 Fig. 10. Reactive power supplied by the power supply considering the unbalanced load currents shown in Fig. 7 and the different multi-  
 372 objective optimization criteria.

373

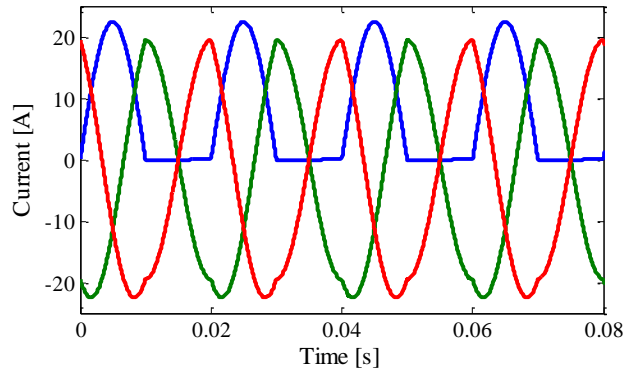
374

## 375 *B. Balanced Non-linear Load*

376 To evaluate the performance of the proposed control system and to compensate for harmonic distortion in  
377 the load currents, a non-linear load was implemented using a rectifier diode in serial connection with a  
378 phase of a star-connected load composed of  $10 \Omega$  resistors. Fig. 11 shows the load current waveforms. For  
379 the distortion introduced by the rectifier diode, as depicted in Table III, the THD in that phase is  
380 approximately 43.35%. Fig. 12 shows the current waveforms at the power supply side for the different  
381 Pareto conditions. Fig. 12(a) shows the current for the closest-to-the-origin criterion, where this signal has a  
382 mean THD of 5.59%; Fig. 12(b) shows the waveforms corresponding to the restriction condition  $|e_Q| < 200$   
383 [VAR], where the signal has a THD of approximately 5.73%; Fig. 12(c) illustrates the waveform for the  
384 power supply currents corresponding to  $|e_Q| < 100$  [VAR], with a THD of 6.80%; finally, Fig. 12(d) shows  
385 the waveforms corresponding to  $|e_Q| < 50$  [VAR], with a THD of 7.36%. From these results, it can be  
386 concluded that the THD is higher when the reactive power is very restricted (see Fig. 12(c)). Finally, Table  
387 III includes results using the three different multi-objective optimization criteria studied in this work. In  
388 this table, the THD of the supply currents before and after the activation of the active power filter is  
389 provided.

390 Fig. 13 shows the waveforms of the currents supplied by the active power filter, confirming that the  
391 currents are more distorted when the error bands for the reactive power are smaller. Indeed, more distortion  
392 is observed in the waveforms corresponding to  $|e_Q| < 50$  [VAR] (see Fig. 13(d)).

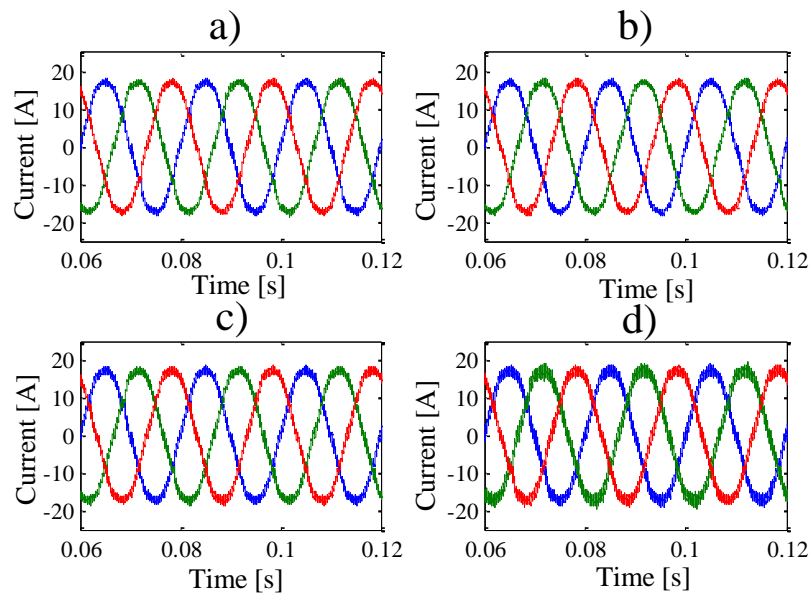
393 Fig. 14 shows the simulation results for the reactive power supplied by the power supply, considering  
394 all the Pareto conditions tested in this work. These results show that there are points where the Pareto  
395 conditions are not met with the reactive power exceeding the pre-defined limits. Therefore, the proposed  
396 control system allows the multi-objective problem to be solved using "soft constraints", i.e., in some  
397 operating points, the MO-M<sup>2</sup>PC algorithm selects the best solution among all the available options.



398

399 Fig. 11. Non-linear load current used to verify the performance of the active power filter for compensating distorted currents.

400



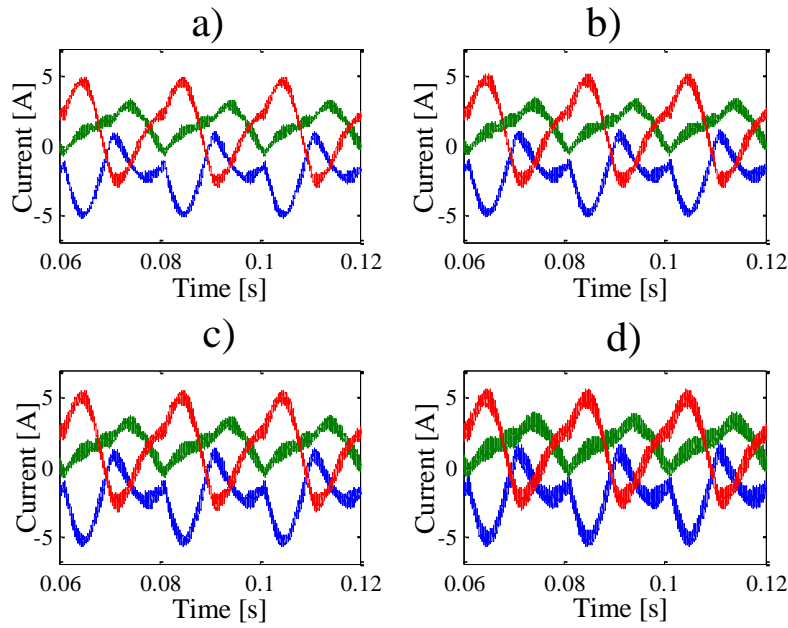
401

402 Fig. 12. Performance of the currents in the power supply for the proposed control system for a non-linear load: a) near-origin criterion; b)  $|e_Q| < 200$  [VAR]; c)  $|e_Q| < 100$  [VAR]; d)  $|e_Q| < 50$  [VAR].

404

405

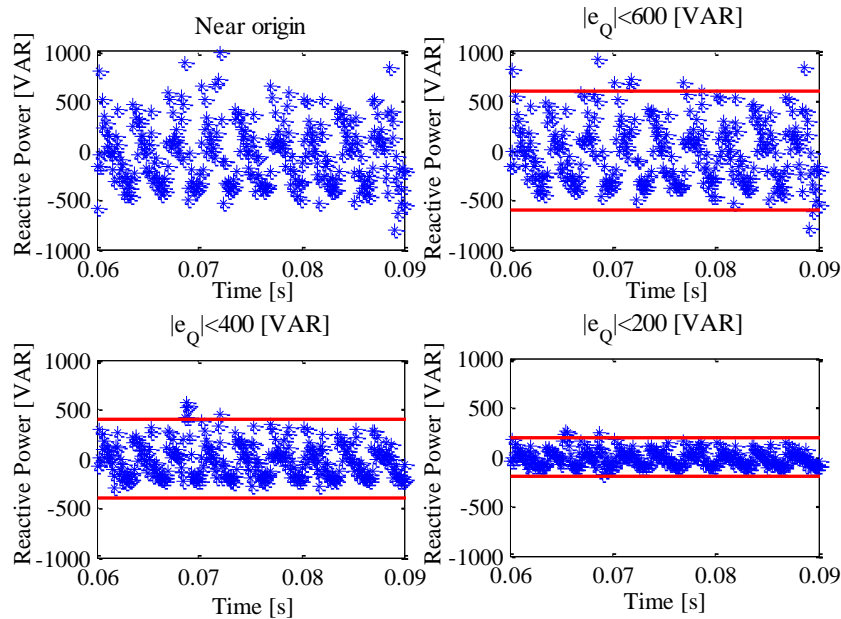




406

407 Fig. 13. Waveforms of the currents supplied by the SAPF corresponding to the non-linear load shown in Fig. 11: a) near-origin criterion; b)  $|e_Q|$   
 408  $< 200$  [VAR]; c)  $|e_Q| < 100$  [VAR]; d)  $|e_Q| < 50$  [VAR].

409



410

411 Fig. 14. Reactive power for an unbalanced load using different multi-objective optimization criteria.

412 In Table III, the THD produced corresponding to each multi-objective criterion is summarized. Note that  
 413 before connecting the SAPF, the THD values are large (particularly in phase *a*), given the strong non-linear  
 414 nature of the load. After connecting the SAPF, the THD is reduced considerably. The results obtained for

415 the near-to-the-origin criterion have a lower THD because there are fewer constraints for the solutions of  
 416 the problem.

417

418 TABLE III: Fundamental current before and after connecting the SAPF for a non-linear load

		Near origin	$ e_Q  < 200$ [VAR]	$ e_Q  < 100$ [VAR]	$ e_Q  < 50$ [VAR]
Phase	THD [%]	THD [%]			
	Before SAPF	After SAPF			
<i>a</i>	43.35	5.55	5.59	6.74	7.25
<i>b</i>	12.04	5.60	5.72	6.78	7.44
<i>c</i>	12.04	5.62	5.88	6.88	7.38

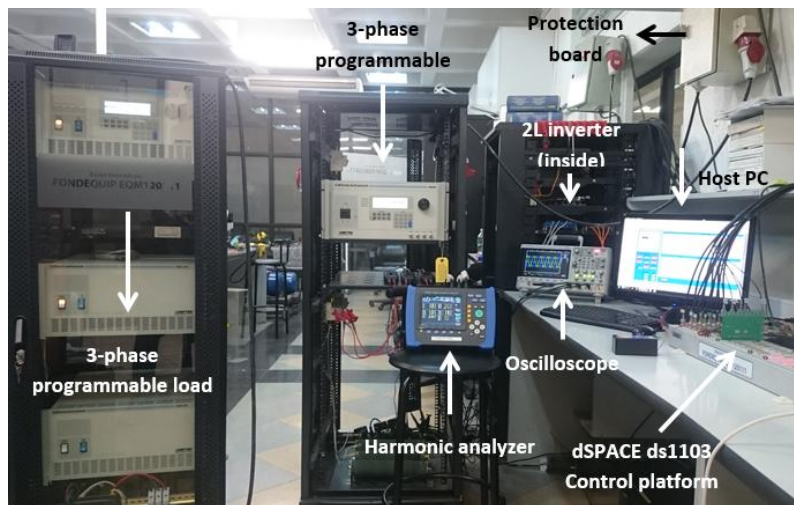
419

420

421

## 422 VI. Experimental Validation

423 To validate the proposed Pareto-based MO-M<sup>2</sup>PC method shown in Fig. 4 and Fig. 6, the experimental  
 424 system shown in Fig. 15 is utilized. The hardware that emulates the behaviour of the power source is a 3-  
 425 phase programmable power supply (manufactured by California Instruments). An Ametek three-phase  
 426 programmable load of 9 kW is used to synthesise linear/non-linear load current profiles. The control  
 427 scheme for the inverter is implemented on a dSPACE DS1103 control platform using the graphical  
 428 software interface Control Desk. Since the execution time of the proposed Pareto-based MO-M<sup>2</sup>PC (see  
 429 Fig. 4 and Fig. 6) is close to 86 [μs] (taking into account the time used for the measurements and external  
 430 calculations), the switching frequency of the experimental setup is set to 10 kHz. This value implies that the  
 431 proposed scheme is executed in one cycle.



432

433 Fig. 15. Experimental Setup.

434 The parameter values used in the experiments are the same as those used to obtain the simulation results  
 435 discussed in Section V. These values are a three-phase AC voltage of 85 [V<sub>rms</sub>], the dc-link voltage of 400  
 436 [V] and filter inductances of 5 [mH] used to interface the power converter to the PCC. In addition, the load  
 437 is interfaced to the PCC using inductances of 2.5 [mH]. A switching frequency of 10 [kHz] is used in the  
 438 experimental system to implement the Pareto-based control system. For recording current and voltage  
 439 signals, the digital scope KEYSIGHT - InfiniVision DSO-X 3024T is used. Furthermore, for the analysis of  
 440 the harmonic spectrum, a HIOKI 3196 power analyser is used.

441 Experimental tests considering the same criteria reported in Section V, i.e., closest-to-the-origin criterion  
 442 and constraint on the reactive power error  $|e_Q| = |Q_s - Q_s^*|$ , were performed in this section. Furthermore,  
 443 similar loads to those utilized in Section V were used for the experimental tests. Therefore, to evaluate the  
 444 effectiveness of the proposed MO-M<sup>2</sup>PC, experimental tests were performed for two disturbance scenarios:  
 445 connection of an unbalanced linear load and connection of a balanced non-linear load. Thus, the controller  
 446 to compensate for imbalances and harmonic distortion was tested for different multi-objective criteria.

#### 447 A. Unbalanced Linear Load

448 To evaluate the performance of the proposed control system to compensate for unbalanced systems,  
 449 unbalanced 3-wire resistive loads of 17.5 Ω, 14 Ω and 8 Ω were programmed in the 3φ load (see Fig. 16).

450 The performance of the Pareto-based MO-M<sup>2</sup>PC considering different criteria for compensating a linear  
451 unbalanced system is shown in Fig. 17.

452 The results show that the closest-to-the-origin criterion produces load waveforms with low distortion (see  
453 Fig. 17(a)). The frequency spectrum corresponding to the waveforms shown in Fig. 17(a) is shown in Fig.  
454 17€. Note that most of the harmonics are concentrated in the high-frequency region ( $n=200$ ) corresponding  
455 to the side bands produced by the switching frequency ( $f_s=10$  kHz). As the error band  $Q$  decreases, the  
456 distortion in the waveforms increases (see Fig. 17(b)-(d)). This result is produced because (as  
457 aforementioned) for a smaller error band, there are fewer switching states that can be applied (see Fig. 5).  
458 Moreover, the states selected within the Pareto front are not necessarily optimal considering the near-to-  
459 the-origin criterion. If the error band is large (see Fig. 17(b)), the produced waveforms are similar to those  
460 shown in Fig. 17(a). This result matches the simulation results discussed in Section V and the fact that for a  
461 large error band, the closest-to-the-origin switching state can be selected. Finally, related to the  
462 performance shown in Fig. 17, Table IV shows the results for the different multi-objective optimization  
463 criteria studied in this work. In this table, the THD of the supply currents before and after the activation of  
464 the active power filter is provided.

465 Fig. 18 shows the compensating currents supplied by the active power filter. As expected, the SAPF  
466 injects the unbalanced components of the load current (see Fig. 16). The distortion and ripple in these  
467 current components increase depending on the error band used in the Pareto-based control algorithm.  
468 Similar to the simulation results, the experimental results show more distortion in the waveforms  
469 corresponding to  $|e_Q| < 50$  [VAR] [see Fig. 18(d)]. The experimental results depicted in Fig. 17-Fig. 19 are  
470 in broad agreement with those obtained in Section V, Simulation Results, Fig. 8-Fig. 10.

471 To verify the performance of the multi-objective criteria for achieving reactive power restriction, the data  
472 captured by the analogue-to-digital converters (ADC) available in the dSPACE DS1103 control platform  
473 are plotted in Fig. 19. The closest-to-the-origin criterion for reactive power has a similar behaviour to that  
474 achieved when the error of the reactive power is restricted to a value of  $|e_Q| < 200$  [VAR]. When the

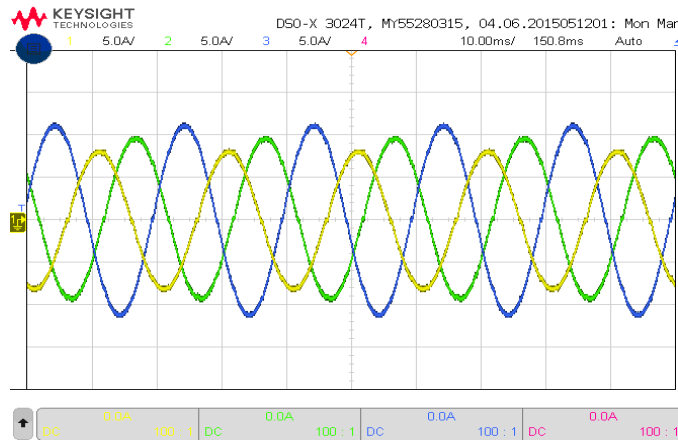
475 restriction is more stringent and the error is maintained inside the values corresponding to  $|e_Q| < 100$  [VAR],  
 476 the system still obtains a reasonable performance in terms of power quality (THD in the current below 5%),  
 477 and the reactive power is similar to that obtained using the closest-to-the-origin criterion. However, when  
 478 the error is further restricted to  $|e_Q| < 50$  [VAR], the THD increases to approximately 6.5% because the space  
 479 of possible solutions is very small. Note that at some points, the reactive power exceeds the threshold, i.e.,  
 480 there is no feasible solution point in that sampling time, and the algorithm searches for the control action  
 481 closer to the constraint (i.e., the constraint behaves as a soft constraint, an issue that was previously  
 482 corroborated using simulations).

483 Table IV shows the values of the fundamental current before and after connecting the SAPF. Initially,  
 484 relatively large unbalanced currents are observed, with a 19.15% difference between the amplitudes of the  
 485 fundamentals in different phases. After compensation, the current is well balanced with an average  
 486 difference of 2.1% between the amplitudes of different phases. Even when the numerical values are not  
 487 exactly the same, the experimental results shown in Table IV are in broad agreement and well correlated  
 488 with the simulation results depicted in Table II.

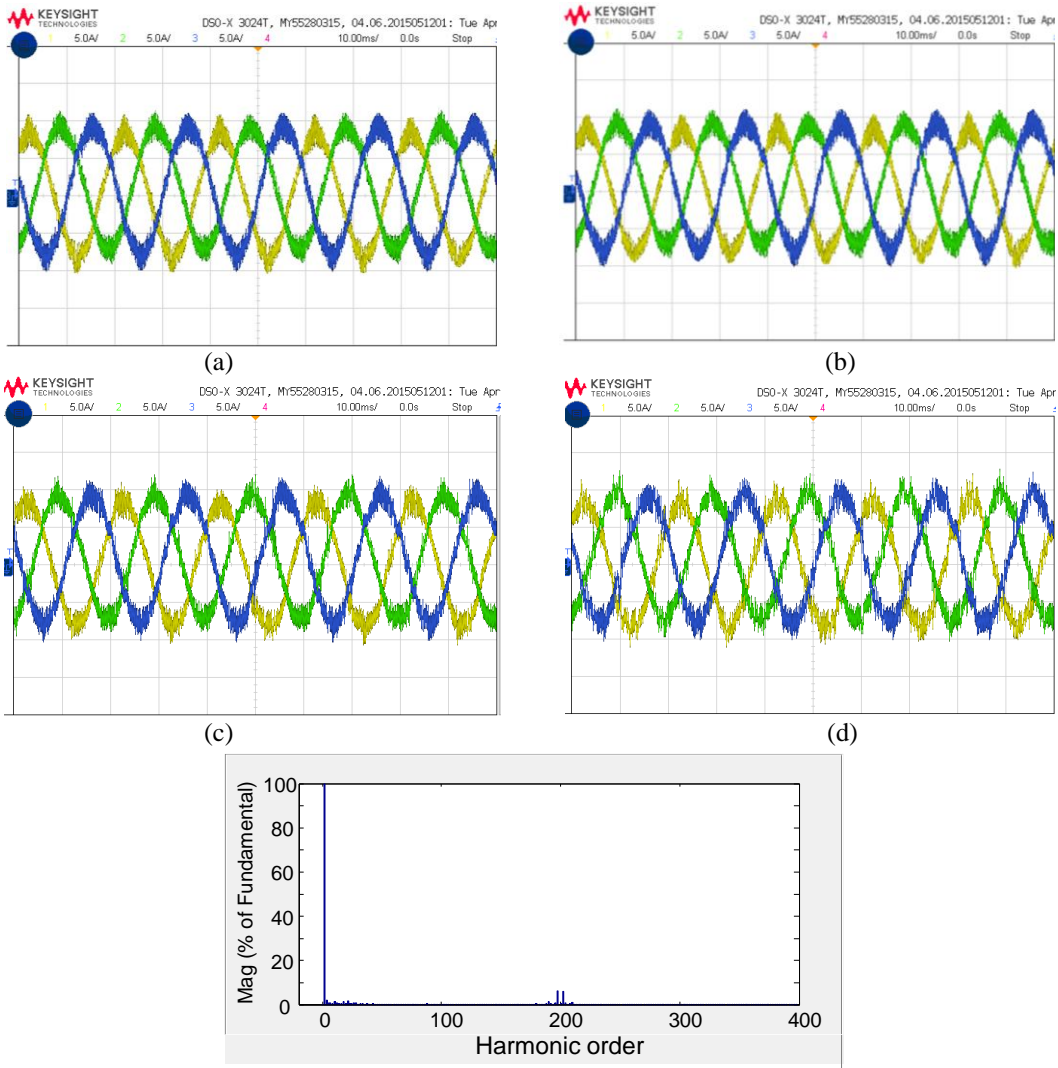
489 TABLE IV: Fundamental current before and after connecting the SAPF for an unbalanced load

		Near origin	$ e_Q  < 200$ [VAR]	$ e_Q  < 100$ [VAR]	$ e_Q  < 50$ [VAR]
Phase	$I_{fund}$ [A]	$I_{fund}$ [A]			
	Before SAPF	After connecting SAPF			
<i>a</i>	5.59	5.58	5.59	5.97	6.47
<i>b</i>	6.68	5.59	5.58	5.76	6.57
<i>c</i>	7.91	5.80	5.83	6.04	6.91

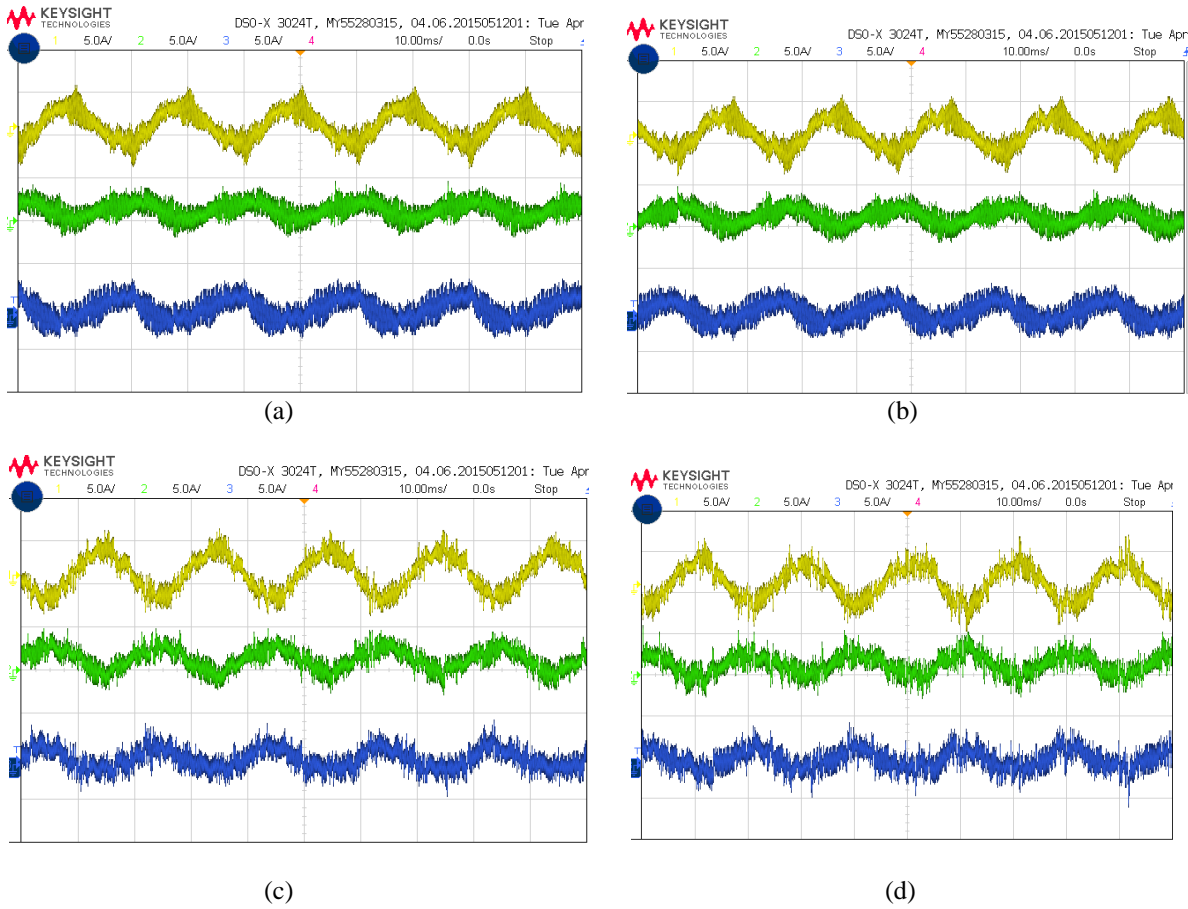
490



491  
492 Fig. 16. Unbalanced load current for compensation (5 A/div - 10 ms/div).



494  
495  
496  
497  
498  
499  
500 Fig. 17. Performance of the currents in the power supply for the proposed control system for an unbalanced load: a) near-origin criterion (5  
501 A/div - 10 ms/div); b)  $|e_Q| < 200$  [VAR] (5 A/div - 10 ms/div); c)  $|e_Q| < 100$  [VAR] (5 A/div - 10 ms/div); d)  $|e_Q| < 50$  [VAR] (5 A/div - 10  
502 ms/div); e) frequency spectrum corresponding to the waveforms shown in Fig. 17(a).



504  
505

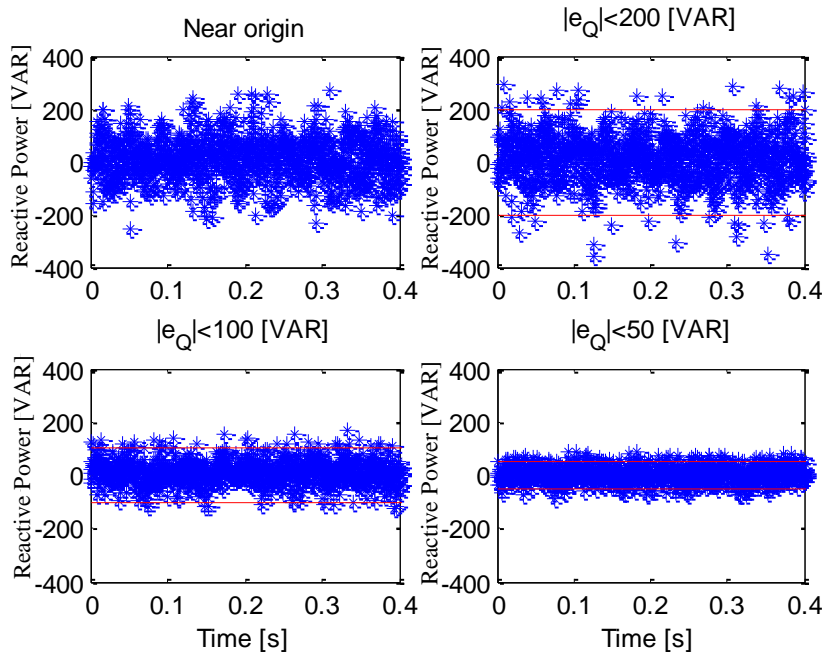
506

507

508

509

Fig. 18. Currents supplied by the SAPF when compensating for the unbalanced currents shown in Fig. 16: a) near-origin criterion (5 A/div – 10 ms/div); b)  $|e_Q| < 200$  [VAR] (5 A/div – 10 ms/div); c)  $|e_Q| < 100$  [VAR] (5 A/div – 10 ms/div); d)  $|e_Q| < 50$  [VAR] (5 A/div – 10 ms/div).



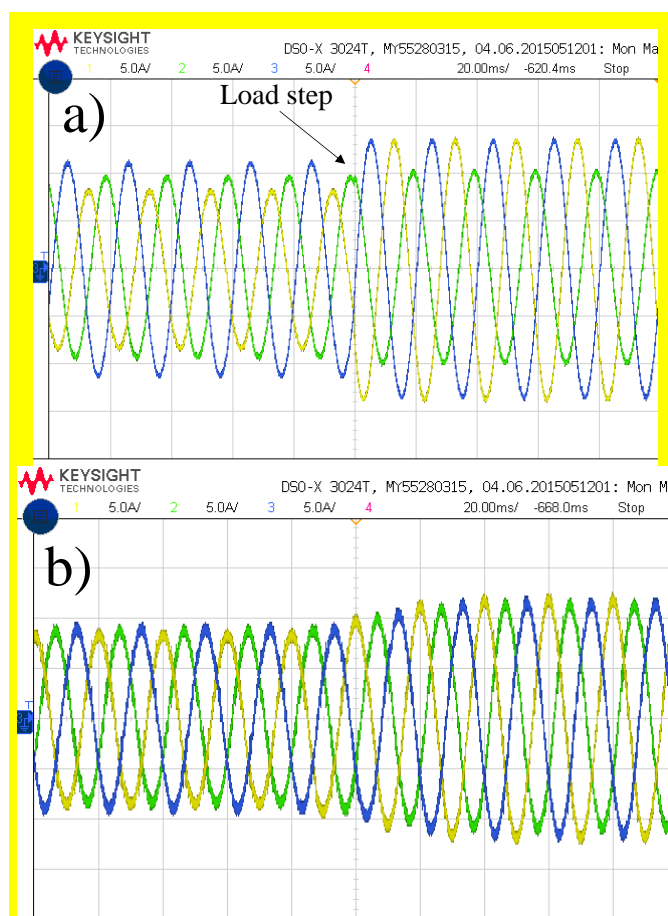
510

511

Fig. 19. Reactive power supplied by the power supply using different multi-objective optimization criteria.

512 Finally, to analyse the transient response of the proposed control scheme, a load step is considered in one  
513 of the phases. To produce this load step, in the experimental setup, the resistance in phase "a" is changed  
514 from 17.5 [ $\Omega$ ] to 8 [ $\Omega$ ], producing an increase in the current of the load. The load step is shown in Fig.  
515 20(a). Fig. 20(b) shows the power supply currents during the load step. From this figure, it can be  
516 concluded that the active power filter compensates for the power supply currents in less than two cycles.  
517 This test was performed with the proposed control scheme operating with the "near-origin" multi-objective  
518 optimization criteria (see Fig. 19).

519



520

521 Fig. 20. Performance of the proposed control system for an unbalanced load step. (a) Load currents. (b) Power supply currents.

522

### 523 B. *Balanced Non-linear Load*

524 To evaluate the performance of the proposed control system for reducing the harmonic distortion in the  
525 power supply currents, a non-linear load was implemented using a star-connected load comprising a 10  $\Omega$

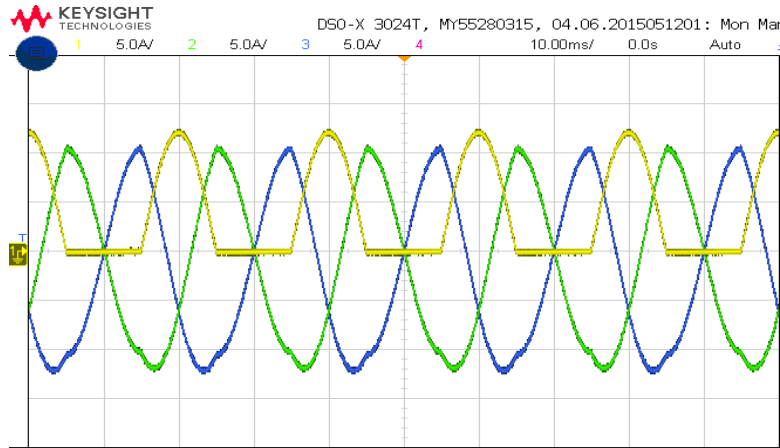


526 resistor per phase. A rectifier diode was serially connected to the resistor in phase  $a$ . Fig. 21 shows the load  
527 current waveforms. Note the distortion introduced by the rectifier diode. As depicted in Table V, the THD  
528 in that phase is approximately 44.48%. Fig. 22(a) shows the compensated waveforms obtained by operating  
529 the Pareto-based MO-M<sup>2</sup>PC using the closest-to-the-origin criterion. In this case, the current has a good  
530 harmonic spectrum with a THD of approximately 5.5%. When the error band is restricted to  $|e_Q| < 200$   
531 [VAR] [see Fig. 22(b)], the obtained performance is very similar to that depicted in Fig. 22(a).  
532 Furthermore, for the non-linear load case, the ripple and THD in the compensated currents are also higher  
533 when the restriction in the reactive power error is further increased to  $|e_Q| < 50$  [VAR]. This effect is  
534 produced because the algorithm is choosing switching states that are not optimal with respect to the closest-  
535 to-the-origin criterion. The computational time required to implement the control strategies has a value  
536 below 86  $\mu$ s for all the compensated currents shown in Fig. 22(a)-(d). Note that the experimental results  
537 depicted in Fig. 22 are in broad agreement with those shown in Fig. 12, Section V. Finally, in Table V, the  
538 THD of the supply currents before and after the activation of the active power filter is provided for the  
539 different multi-objective optimization criteria considered in this work.

540 The compensating currents supplied by the active power filter are shown in Fig. 23. As expected, the  
541 SAPF injects the harmonic and unbalanced components of the load currents (see Fig. 21). As discussed for  
542 the linear unbalanced current case, the distortion and ripple in the currents supplied by the SAPF increase  
543 depending on the error band used in the Pareto-based control algorithm. More distortion is observed in the  
544 waveforms corresponding to  $|e_Q| < 50$  [VAR].

545 To experimentally validate the performance of the control algorithm for restricting the instantaneous  
546 reactive power error, the experimental results captured by the ADC available in the dSPACE platform are  
547 plotted in Fig. 24. When the near-to-the-origin criterion is used, the reactive power is similar to that  
548 obtained when  $|e_Q| < 200$  [VAR], as shown in Fig. 24(b). Moreover, even when a very non-linear load is  
549 used, the reactive power is successfully regulated even for the strong restriction  $|e_Q| < 50$  [VAR], which is  
550 used in the proposed Pareto-based MO-M<sup>2</sup>PC.

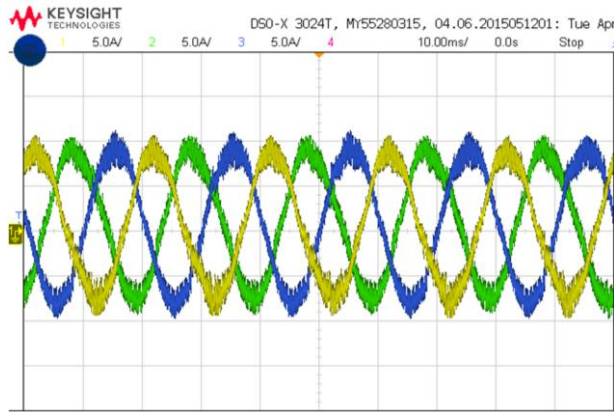
551



552

553 Fig. 21. Non-linear load for compensation (10 ms/div – 5 A/div).

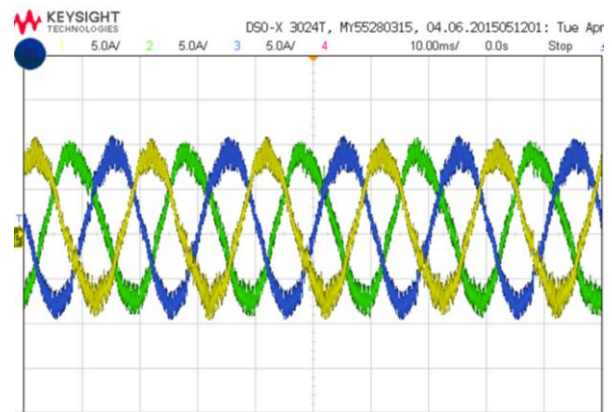
554



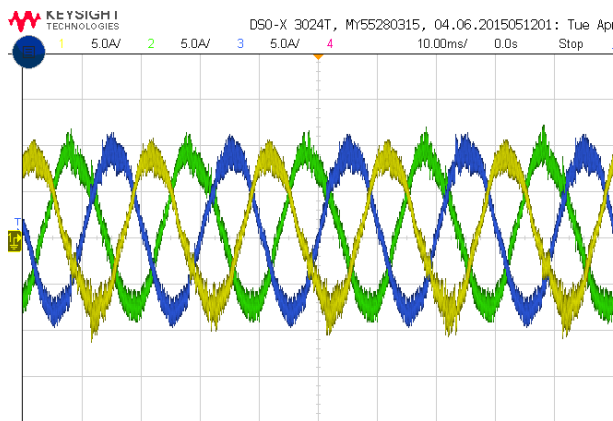
555

556

(a)



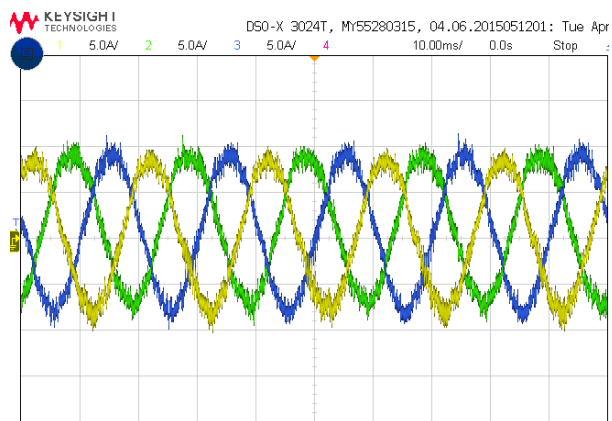
(b)



557

558

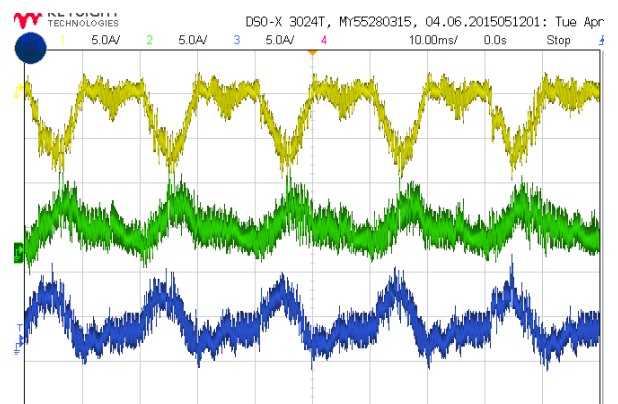
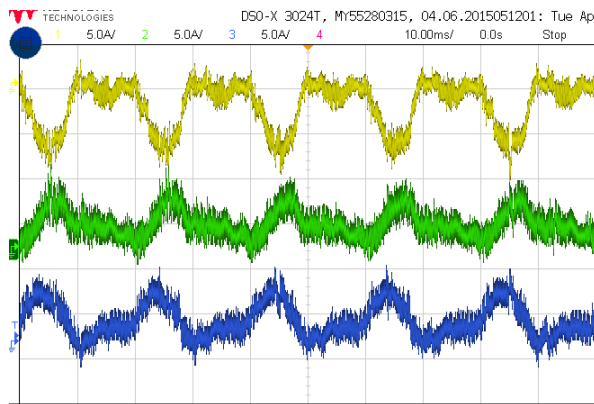
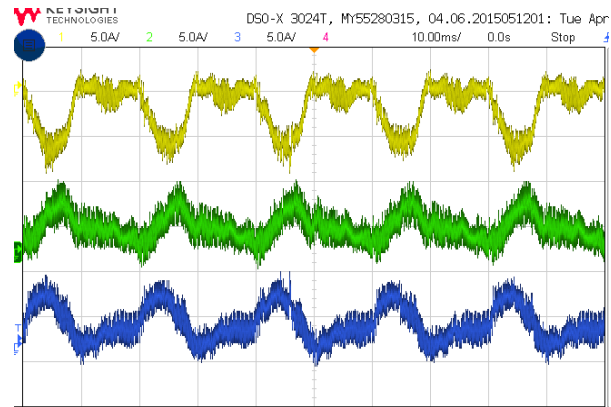
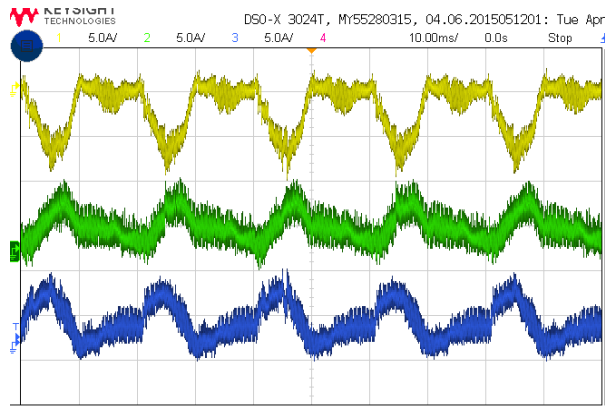
(c)



(d)

559 Fig. 22. Performance of the currents in the power supply for the proposed control system for compensating non-linear loads: a) near-origin  
560 criterion (5 A/div – 10 ms/div); b)  $|e_Q| < 200$  [VAR] (5 A/div – 10 ms/div); c)  $|e_Q| < 100$  [VAR] (5 A/div – 10 ms/div); d)  $|e_Q| < 50$  [VAR] (5  
561 A/div – 10 ms/div).

562



563

564

565

566

567

568

569

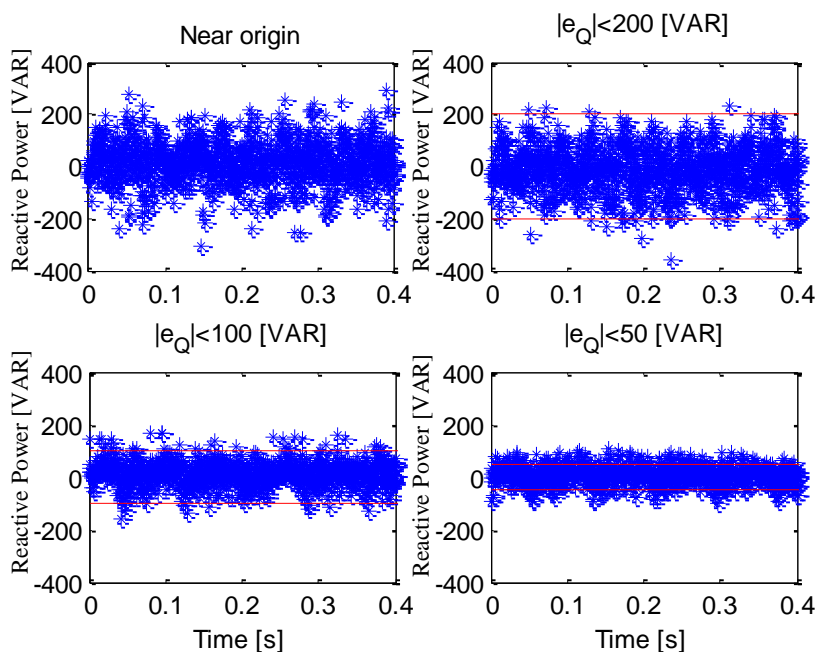
(a)

(b)

(c)

(d)

Fig. 23. Performance of the currents in the inverter for the proposed control system for compensating non-linear loads: a) near-origin criterion (5 A/div - 10 ms/div); b)  $|e_Q| < 200$  [VAR] (5 A/div - 10 ms/div); c)  $|e_Q| < 100$  [VAR] (5 A/div - 10 ms/div); d)  $|e_Q| < 50$  [VAR] (5 A/div - 10 ms/div).



570

571 Fig. 24. Reactive power for non-linear loads using different multi-objective optimization criteria.

572 In Table V, the harmonic content for each multi-objective criterion is summarized. Note that before  
 573 connecting the SAPF, the THD values are large, given the strong non-linear nature of the load. After  
 574 connecting the SAPF, the THD is reduced considerably. The results from the near-to-the-origin  
 575 have a lower THD because there are fewer constraints for the solutions of the problem. Even when the  
 576 numerical values are not exactly the same, the experimental results shown in Table V are in broad  
 577 agreement and correlated with the simulation results depicted in Table III, Section V.

578

579 TABLE V: Power quality before and after connecting the SAPF for a non-linear load

		Near origin	$ e_Q  < 200$ [VAR]	$ e_Q  < 100$ [VAR]	$ e_Q  < 50$ [VAR]
Phase	THD [%]	THD [%]			
	Before SAPF	After SAPF			
<i>a</i>	44.48	5.45	5.46	6.49	7.34
<i>b</i>	11.94	5.76	5.99	6.93	7.90
<i>c</i>	12.00	5.89	5.92	6.72	7.59

580

## 581 VII. Conclusions

582 In this paper, a novel M<sup>2</sup>PC strategy is presented. This strategy is based on the application of a Pareto-  
583 based algorithm using multi-objective optimization. The proposed methodology maintains all the  
584 advantages of conventional MPC, i.e., simplicity for the inclusion of nonlinearities, intuitive formulation  
585 and fixed switching frequency. The experimental results demonstrate that the proposed technique does not  
586 require the use of weighting factors, which are usually difficult to select and tune. Moreover, the  
587 implementations of hard and soft constraints, for instance, in the tracking errors, are relatively simple to  
588 accomplish using this Pareto-based algorithm.

589 The main disadvantage of the proposed methodology is the increased computational burden imposed by  
590 the implementation of the proposed Pareto-based algorithm. However, considering the high processing  
591 power achieved by a relatively low-cost modern digital signal processor (DSP) augmented by field  
592 programmable gate arrays (FPGAs), this disadvantage is not very important.

593 It can be concluded that the time burden of the proposed control scheme is comparable (in relation to the  
594 order of magnitude) to the technique that uses multi-resonant controllers. On the one hand, the  
595 computational requirement of the proposed control scheme is close to 86 [μs]. On the other hand, the  
596 experimental system depicted in Fig. 15 was used to implement a SAPF in [33] [34] based on resonant  
597 controllers. In this case, in each phase, a PI controller and seven resonant controllers were implemented in a  
598 parallel topology. The computational burden of this control scheme is close to 50 [μs].

599 The proposed control strategy produces good performance for power filtering applications. Furthermore,  
600 this strategy is suitable for other applications of power converters, such as grid-connected inverters and  
601 wind energy conversion systems connected to the utility using back-to-back power converters. A new  
602 method to compensate for the delay in M<sup>2</sup>PC is also proposed and validated in this work, considering that a  
603 symmetrical SVM switching pattern is applied.

604 It should be pointed out that, in this work, the output filter for the active power filter corresponds to an L  
605 filter. If this filter is required to inject current with a small ripple, an LCL filter can be placed at the output  
606 of the inverter.

## 607 Acknowledgements

608 The authors would like to thank the financial support of FONDECYT grant number 1170683,  
609 FONDECYT grant number 1180879 and the Complex Engineering Systems Institute (CONICYT – PIA –  
610 FB0816).

611  
612

## 613 References

614

- [1] J. Rodriguez, M. Kazmierkowski, J. Espinoza, P. Zanchetta, H. Abu-Rub, H. A. Young and C. Rojas, "State of the Art of Finite Control Set Model Predictive Control in Power Electronics," *IEEE Transactions on Industrial Informatics*, vol. 9, no. 2, pp. 1003-1016, 2013.
- [2] P. Mc-Namara and P. Milano, "Efficient implementation of MPC-based AGC for real-world systems with low inertia," *Electric Power System Research*, vol. 158, pp. 315-323, 2018.
- [3] E. Bighash, S. Sadeghzadeh, E. Ebrahimzadeh and F. Blaabjerg, "High quality model predictive control for single phase grid-connected photovoltaic inverters," *Electric Power System Research*, vol. 158, pp. 115-125, 2018.
- [4] B. Lekouaghet, A. Boukabou, N. Lourci and K. Bedrine, "Control of PV grid connected systems using MPC technique and different inverter configuration models," *Electric Power System Research*, vol. 154, pp. 287-298, 2018.
- [5] P. Cortes, S. Kouro, B. La Rocca, R. Vargas, J. Rodriguez, J. Leon, S. Vazquez and L. Franquelo, "Guidelines for weighting factors design in Model Predictive Control of power converters and drives," in *IEEE International Conference on Industrial Technology*, Churchill, Victoria, Australia, 2009.
- [6] A. Mora, A. Orellana, J. Juliet and R. Cárdenas, "Model Predictive Torque Control for Torque Ripple Compensation in Variable-Speed PMSMs," *IEEE Transaction on Industrial Electronics*, vol. 63, no. 7, pp. 4584-4592, 2016.
- [7] F. Donoso, A. Mora, R. Cardenas, A. Angulo, D. Saez and M. Rivera, "Finite-Set Model-Predictive Control Strategies for a 3L-NPC Inverter Operating With Fixed Switching Frequency," *IEEE Transactions on Industrial Electronics*, vol. 65, no. 5, pp. 3954-3965, 2018.
- [8] M. Vatani, M. Hovd and M. Molinas, "Finite Control Set Model Predictive Control of a shunt active power filter," in *Twenty-Eighth Annual IEEE Applied Power Electronics Conference and Exposition (APEC)*, Long Beach, CA, USA, 2013.
- [9] T. Geyer, N. Oikonomou, G. Papafotiou and F. Kieferndorf, "Model predictive pulse pattern control," *IEEE Transactions on Industry Applications*, vol. 48, no. 2, pp. 663-676, 2012.
- [10] P. Stolze, P. Landsmann, R. Kennel and T. Mouton, "Finite-set model predictive control with heuristic voltage vector preselection for higher prediction horizons," in *Proceedings of the 2011-14th European Conference on Power Electronics and Applications (EPE 2011)*, Birmingham, United Kingdom, 2011.
- [11] R. G. a. F. Barrero, S. Toral, M. Durán, M. Arahall and J. Mora, "Predictive-space vector PWM current control method for asymmetrical dual three-phase induction motor drives," *IET Electric Power Applications*, vol. 4, no. 1, pp. 26-34, 2010.
- [12] M. Habibullah, D. Lu, D. Xiao and M. Rahman, "Finite-state predictive torque control of induction motor supplied from a three-level NPC voltage source inverter," *IEEE Transactions on Power Electronics*, vol. 32, no. 1, pp. 479-489, 2017.
- [13] K. Antoniewicz, M. Jasinski, M. Kazmierkowski and M. Malinowski, "Model predictive control for three-level four-leg flying capacitor converter operating as shunt active power filter," *IEEE Transactions on Industrial Electronics*, vol. 63, no. 8, pp. 5255-5262, 2016.
- [14] M. Chaves, E. Margato, J. Silva, S. Pinto and J. Santana, "Fast optimum-predictive control and capacitor voltage balancing strategy for bipolar back-to-back npc converters in high-voltage direct current transmission systems," *IET Generation, Transmission Distribution*, vol. 5, no. 3, pp. 368-375, 2011.
- [15] R. O. Ramírez, J. R. Espinoza, F. Villarroel, E. Maurelia and M. E. Reyes, "A novel hybrid finite control set model predictive control scheme with reduced switching," *IEEE Transactions on Industrial Electronics*, vol. 61, no. 11, pp. 5912-5920, 2014.

- [16] P. Cortes, J. Rodriguez, D. Quevedo and C. Silva, "Predictive current control strategy with imposed load current spectrum," *IEEE Transactions on Power Electronics*, vol. 23, no. 2, pp. 612-618, 2008.
- [17] A. Bouafia, J. Gaubert and F. Krim, "Predictive direct power control of three-phase pulsewidth modulation (pwm) rectifier using space-vector modulation (svm)," *IEEE Transactions on Power Electronics*, vol. 25, no. 1, pp. 228-236, 2010.
- [18] H. T. Nguyen, E. Kim, I. Kim, H. Choi and J. Jung, "Model Predictive Control with Modulated Optimal Vector for a Three-Phase Inverter with an LC Filter," *IEEE Transactions on Power Electronics*, vol. 33, no. 3, pp. 2690-2703, 2018.
- [19] S. Yeoh, T. Yang, L. Tarisciotti, C. Hill, S. Bozhko and P. Zanchetta, "Permanent-Magnet Machine-Based Starter-Generator System With Modulated Model Predictive Control," *IEEE Transactions on Transportation Electrification*, vol. 3, no. 4, pp. 878-890, 2017.
- [20] L. Tarisciotti, J. Lei, A. Formentini, A. Trentin, P. Zanchetta, P. Wheeler and M. Rivera, "Modulated Predictive Control for Indirect Matrix Converter," *IEEE Transactions on Industry Applications*, vol. 5, pp. 4644-4654, 2017.
- [21] L. Tarisciotti, P. Zanchetta, A. Watson, S. Bifaretti and J. Clare, "Modulated Model Predictive Control for a Seven-Level Cascaded H-Bridge Back-to-Back Converter," *IEEE Transactions on Industrial Electronics*, vol. 61, no. 10, pp. 5375-5383, 2014.
- [22] R. Rabbeni, L. Tarisciotti, A. Gaeta, A. Formentini, P. Zanchetta, M. Pucci, M. Degano and M. Rivera, "Finite states modulated model predictive control for active power filtering systems," in *Energy Conversion Congress and Exposition (ECCE)*, Montreal, QC, Canada, 2015.
- [23] M. Rivera, M. Perez, C. Baier, J. Munoz, V. Yaramasu, B. Wu, L. Tarisciotti, P. Zanchetta and P. Wheeler, "Predictive Current Control with fixed switching frequency for an NPC converter," in *IEEE 24th International Symposium on Industrial Electronics (ISIE)*, 2015.
- [24] L. Tarisciotti, P. Zanchetta, A. Watson, J. Clare, M. Degano and S. Bifaretti, "Modulated Model Predictive Control for a Three-Phase Active Rectifier," *IEEE Transactions on Industry Applications*, vol. 51, no. 2, pp. 1610-1620, 2015.
- [25] S. S. Yeoh, T. Yang, L. Tarisciotti, S. Bozhko and P. Zanchetta, "Hybrid modulated model predictive control for the more electric aircraft generator system," in *International Conference on Electrical Systems for Aircraft, Railway, Ship Propulsion and Road Vehicles (ESARS)*, Aachen, Germany, 2015.
- [26] L. Tarisciotti, F. A., A. Gaeta, M. Degano, P. Zanchetta, R. Rabbeni and M. Pucci, "Model Predictive Control for Shunt Active Filters With Fixed Switching Frequency," *IEEE Transactions on Industry Applications*, vol. 53, no. 1, pp. 296-304, 2017.
- [27] F. Villarroel, J. R. Espinoza, C. Rojas, J. Rodriguez, M. Rivera and D. Sbarbaro, "Multiobjective Switching State Selector for Finite-States Model Predictive Control Based on Fuzzy Decision Making in a Matrix Converter," *IEEE Transactions on Industrial Electronics*, vol. 60, no. 2, pp. 589 - 599, 2013.
- [28] C. A. Rojas, J. Rodriguez, F. Villarroel, J. R. Espinoza, C. A. Silva and M. Trincado, "Predictive Torque and Flux Control Without Weighting Factors," *IEEE Transactions on Industrial Electronics*, vol. 60, no. 2, pp. 681-690, 2013.
- [29] C. Rojas, J. Rodriguez, F. Villarroel, J. Espinoza and D. Khaburi, "Multiobjective Fuzzy Predictive Torque Control of an induction motor drive," in *Power Electronics, Drives Systems Technologies Conference (PEDSTC), 2015 6th*, Tehran, Iran, 2015.
- [30] D. E. Quevedo, R. P. Aguilera, M. A. Perez, P. Cortes and R. Lizana, "Model Predictive Control of an AFE Rectifier With Dynamic References," *IEEE Transactions on Power Electronics*, vol. 27, no. 7, pp. 3128-3136, 2012.
- [31] G. Bode, P. Loh, M. Newman and D. Holmes, "An improved robust predictive current regulation algorithm," *IEEE Transactions on Industry Applications*, vol. 41, no. 6, pp. 1720-1733, 2005.
- [32] P. Cortes, J. Rodriguez, C. Silva and A. Flores, "Delay Compensation in Model Predictive Current Control of a Three-Phase Inverter," *IEEE Transactions on Industrial Electronics*, vol. 59, no. 2, pp. 1323-1325, 2012.
- [33] C. Burgos-Mellado, C. Hernández-Carimán, R. Cárdenas, D. Sáez, M. Sumner, A. Costabeber and H. K. Morales Paredes, "Experimental Evaluation of a CPT-Based Four-Leg Active Power Compensator for Distributed Generation," *IEEE Journal of Emerging and Selected Topics in Power Electronics*, vol. 5, no. 2, pp. 747 - 759, 2017.
- [34] C. J. H. Cariman, "Control de un filtro activo paralelo basado en un conversor fuente de voltaje de 4-piernas aplicado a sistemas de distribución de 4-hilos," Master thesis of the University of Chile, Santiago, Chile, 2016.
- [35] C. Burgos-Mellado, . R. Cárdenas, S. Doris, . A. Costabeber and M. Sumner, "A Control Algorithm Based on the Conservative Power Theory for Cooperative Sharing of Imbalances in 4-Wire Systems," *IEEE Transactions on Power Electronics*, p. DOI: 10.1109/TPEL.2018.2869866, 2018.